Measurement of Blood Flow and Assessment of Breast Health by Using Non-Invasive Optical Techniques

por

Noemi Jasmin Salazar Hermenegildo

Tesis sometida como requisito parcial para obtener el grado de

DOCTOR EN CIENCIAS EN LA ESPECIALIDAD DE ÓPTICA

en el

Instituto Nacional de Astrofísica, Óptica y Electrónica

Noviembre 2015

Tonantzintla, Puebla

Supervisada por:

Dr. Julio Cesar Ramírez San Juan
Investigador Titular INAOE
Dr. Lothar Lilge
Senior Scientist Princess Margaret Cancer Center

©INAOE 2015
El autor otorga al INAOE el permiso de reproducir y distribuir copias en su totalidad o en partes de esta tesis

Abstract

Laser Speckle Imaging (LSI) is an optical technique used to generate blood flow maps with high spatial and temporal resolution. A modified laser speckle imaging (mLSI) enables computation of blood flow maps with relatively high spatial resolution. Although it is known that the sensitivity and noise in LSI measurements depend on image exposure time, a fundamental disadvantage of mLSI is that it does not take into account this parameter. In this thesis, the exposure time into the mLSI method was integrated and provides experimental support for this approach with measurements from an in vitro flow phantom. In the other hand it is well known that in LSI, the speckle size must exceed the Nyquist criterion to maximize the speckle's pattern contrast. The effect of speckle-pixel size ratio not only in dynamic speckle contrast, but also on the calculation of the relative flow speed for temporal and spatial analysis was studied as well. Data suggest that the temporal LSCI algorithm is more accurate at assessing the relative changes in flow speed than the spatial algorithm. Quantify the probabilities for women to develop breast cancer in the future or harbour breast cancer, via their bulk optical tissue properties is the objective of the clinical research in the Ontario Cancer Institute, Canada. As a part of this research, based on measurements of trans-illumination spectroscopy breast tissue from participants of the clinical research, hemoglobin, oxygenated hemoglobin, collagen, lipids and water concentration and the scattering value were obtained by using the equation diffusion in this thesis work.

Agradecimientos

Quiero agradecer al Dr. Julio Cesar por la confianza puesta en mí y permitirme ser parte de su grupo de trabajo. Porque con su gran capacidad de transimir el conocimiento fue posible que las ideas se materializaran en este trabajo.

Un agradecimiento especial para el Dr. Lothar Lilge por permitirme trabajar dentro de su grupo, por todo su apoyo durante mi estancia en el Princess Margaret Hospital. Sin duda el ejemplo de una persona con gran calidad humana y que puedo decir fue mi asesor.

Al jurado por revisar este trabajo.

En un país como México es imperante agradecer a todos aquellos que creen en que la ciencia es parte esencial de nuestro desarrollo y proveyeron los recursos económicos que obtuve a través de CONACyT para realizar este trabajo.

Agradezco a una compañera de trabajo que se torno en una gran amiga; Margarita. Por su ayuda incondicional en todo momento y por las alegrías que compartió conmigo durante nuestra estancia en Toronto.

A mi esposo le digo gracias por todo lo que él merece.

Para mis Itztlis, Mi madre, Mis hermanos de sangre y políticos, Mis sobrinos y para todo aquel que le interese este trabajo.

Contents

Contents **i**

1 Introduction **1**
1.1 Motivation . . . 1
1.2 Optical Properties of Biological Tissue . . . 2
1.3 Laser Speckle Imaging . . . 4
1.4 Objectives . . . 5
1.5 Thesis Overview . . . 6

2 Theory **8**
2.1 Speckle pattern . . . 8
2.2 Statistical properties of random light . . . 9
2.2.1 Optical Intensity . . . 9
2.2.2 Temporal Coherence . . . 10
2.2.3 Spatial Coherence . . . 13
2.3 Random Phasor Sum . . . 13
2.4 Speckle Size . . . 16
2.5 Statistical Properties of Time Integrated Intensity . . . 18
2.5.1 Integrated Intensity from only Dynamic Scatterers . . . 18
2.5.2 Average of Time Integrated Intensity . . . 18
2.5.3 Variance of the Time Integrated Intensity . . . 19
2.5.4 Integrated intensity from Static and Dynamic Scatterers . . . 20
2.6 Multiple Speckle Patterns . . . 22
2.7 Velocity of the Scatters . . . 25
2.8 Methods for Laser Speckle Contrast Analysis . . . 26
2.8.1 Spatial Analysis of Laser Speckle Images . . . 26
2.8.2 Temporal Analysis of Laser Speckle Images . . . 27
2.9 LSI versus mLSI . . . 28

3 Integration of Image Exposure Time into a Modified Laser Speckle Imaging Method **29**
3.1 Theory . . . 29
3.2 Experimental design . . . 31

3.2.1 LSI instrument . . . 31
3.2.2 In vitro flow phantom . . . 32
3.2.3 Experiments . . . 32
3.2.4 mLSI image analysis . . . 32
3.3 Results . . . 33
3.3.1 Camera exposure time needs to be considered with mLSI analysis 33
3.3.2 Incorporation of the exposure time in the mLSI model improves substantially the accuracy of this method to measure relative flow rate changes. . . . 34
3.4 Conclusions . . . 36

4 Effects of speckle/pixel size ratio on temporal and spatial speckle-contrast analysis of dynamic scattering systems: Implications for measurements of blood-flow dynamics 38
4.0.1 Flow phantom . . . 39
4.0.2 Laser speckle contrast imaging (LSCI) . . . 39
4.1 Experimental design and data analysis . . . 40
4.2 Results and Discussion . . . 40
4.3 Conclusions . . . 44

5 Trans-illumination Breast Spectroscopy System TiBS for the assessment of breast health 45
5.1 Introduction . . . 45
5.2 Breast cancer statistics . . . 45
5.3 Motivation . . . 48
5.4 Breast anatomy . . . 48
5.5 Breast cancer . . . 48
5.6 Breast Imaging Tests . . . 49
5.7 Optical breast tests . . . 50
5.7.1 Light propagation in biological tissue . . . 51
5.7.2 Chromophore concentration . . . 52
5.8 Methods . . . 53
5.9 F(λ) calculation . . . 54
5.10 TiBS set up and Data Collection . . . 55
5.11 Data correction . . . 55
5.12 Partial Results . . . 56
5.13 Conclusion . . . 59

A Mammography physics 60
A.0.1 Compton effect . . . 60
A.0.2 Photoelectric effect . . . 62

List of Figures 67

List of Tables **70**

Bibliography **71**

Chapter 1

Introduction

This chapter introduces the objective of this project: measurement of blood flow using non-invasive optical techniques.
In Section 1.1 a synopsis of the project is given, establishing the clinical need for non-invasive blood flow monitoring and the technique for its analysis by using Laser Speckle Imaging (LSI). Section 1.2 discusses the biophysical background pertinent to the primary application of this method, the measurement of blood flow. In Section 1.3 the technique of laser speckle imaging is introduced, discussing the currents methods for speckle images analysis, and its suitability as a technique for blood flow monitoring. In Section 1.4 the objectives of this project are established. Finally, Section 1.5 summarizes the details of the subsequent chapters in this thesis, highlighting the development of the project towards its goal.

1.1 Motivation

The blood supply to and from the capillaries is critical because the capillaries are the site of exchange of nutrients and waste products between the vascular and interstitial compartments [1, 2]. For example in the brain, too much blood (hyperemia) may increase intracranial pressure, which can compress and damage delicate brain tissue. In the other hand ischemia occurs when blood flow insufficiency (decreased oxygen and glucose), which begins abruptly or slowly [1]. Death of brain tissue occurs when the flow drops abruptly. Measurement of blood flow in retina is also important. The retinal artery carries blood with oxygen to the retina. When there is a blockage in the main artery of the retina or in one of the small branches, the cells of the light-sensitive retina gradually begin to down due to lack of oxygen. If the normal circulation in the retina is not immediately restored, these cells die within minutes or hours depending on the extent of the blockage of blood flow [2]. This can cause permanent loss of vision and often significant. A variety of techniques have been developed to monitor retinal blood flow. One of the most employed is the Doppler effect to measure the velocity, volume, and flux of blood through the capillaries and larger vessels of the optic nerve head and

superficial retina [3]. In the laser Doppler technique, the frequency of reflected laser light changes when scattered by red blood cells moving through vessels [6]. A two-dimensional picture of blood flow can be obtained by laser Doppler, the laser beam is scanned across the surface of the retina, yielding laser Doppler measurements at multiple points. Two-dimensional images of retinal blood flow can also be obtained using a related technique, LSI which is an alternative laser based, non-invasive blood flow monitoring technique that offers rapid and high resolution images of tissue [7]. The need for a non-invasive technique of monitoring blood flow has arisen and are of great interest in all fields of applied physics. Among the non-invasive methods, optical methods are of particular interest because they allow performing different measurements without physical contact between the measuring apparatus and the sample.
The technique LSI has become well-established as a non-invasive method of monitoring blood flow in brain [7, 8], retina [9, 10] and skin [11, 13, 12]. The relatively low absorption laser light in biological tissue allows the light to penetrate the skin and skull layers to sample the brain tissue beneath. Next section discusses this in more detail.

1.2 Optical Properties of Biological Tissue

Biological tissue is a multilayer medium containing various inclusions, such as, blood vessels. Different processes can take place when light interacts with biological tissue but there are tree fundamental process that will take a place. These will depend on the intensity of photons, their wavelength and the kind of tissue it interacts with. In a simple picture, figure 1.1, if the energy of the photon matches the difference between the energy levels in the tissue molecule it will be absorbed otherwise if the energy of the photon does not match the difference between the energy levels in the tissue molecule the photon might get scattered. Also a certain amount of the photons will be reflected by the tissue surface either a specularly or scattered way.

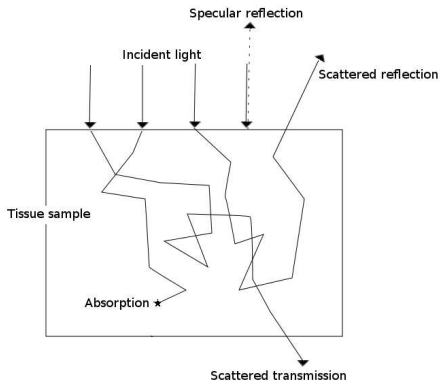

Figure 1.1: Schematic illustration of photons reflection, absorption scattering and transmission in a tissue sample.

Within tissue optics, absorption is defined as the probability for a photon to be absorbed per unit length, it is quantified by the absorption coefficient (μ_a) given in cm^{-1} or mm^{-1}. Tissue component that absorb light are called chromophores. The most important chromophores in the visible and NIR region of the electromagnetic spectrum are haemoglobin and water. The absorption of light by blood depends on the oxygenation, figure 1.2. The energy gained by the tissue absorption of light is involved in several process. It may be re-emitted as a fluorescence, contribute to photochemical reaction, or be redistributed among the molecules as heat, inducing a temperature increasing [4]. In biological tissue scattering is much higher than absorption, as can be seen in figure 1.2.

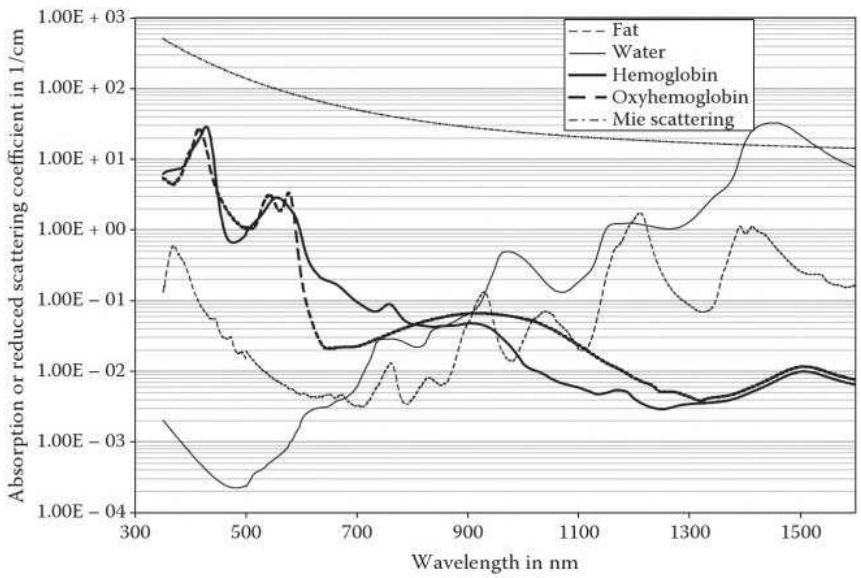

Figure 1.2: Comparison of fourth most common absorbers in tissue and the Mie scattering [5].

Scattering within the tissue depends on the wavelength λ of the light, and particle size a it interacts with. For $a \ll \lambda$ the scattering is termed Rayleigh scattering and for $a \geq \lambda$ the scattering is termed Mie scattering. The scattering in tissue is generally not isotropic. Mie scattered light is more forward scattered, the information about the scattering anisotropy is contained in the anisotropy factor (g) defined as

$$\mu_s' = (1 - g)\mu_s \tag{1.1}$$

given in cm^{-1} or mm^{-1} and where scattering coefficient (μ_s) defined as the probability for a scattering event to occur per unit length. The value of g ranges from -1 to +1 where -1 corresponds to total backscattering and +1 corresponds to total forward scattering. g=0 means isotropic scattering or Rayleigh scattering. A comparison between the μ_a and μ_s coefficients of the blood components is shown in figure 1.2. Scattering

process dominates over absorption which means that light will interact with the blood components in a non-invasive way in a wide interval of wavelengths. Scattered photons for a tissue volume are of major importance for imaging through turbid media. Next section present the LSI as a non-invasive blood flow technique. 1.3.

1.3 Laser Speckle Imaging

It is called speckle to a random intensity distribution formed when the coherent light is scattered by a turbid media on the scale of the wavelength [15]. Considering biological tissue as a turbid media, when it is illuminated with coherent light the scattering by inhomogeneities of tissue volume results in a random change of the phase of waves that are capable of interfering. In a image screen a large number of small bright and darks spots distributed at random are seen. This structure is known as speckle, fugure 1.3.

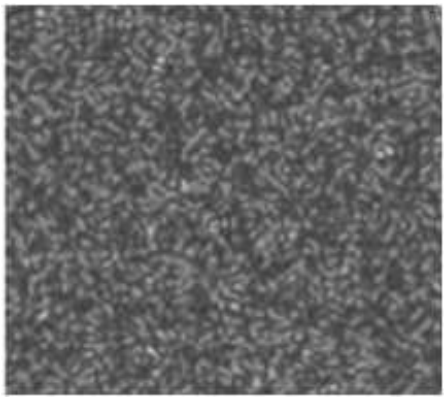

Figure 1.3: Sinple image of speckle pattern.

If the scattering inhomogeneities within the medium are in motion this speckle pattern fluctuations in time, whereas if the scattering inhomogeneities are static the speckle pattern remains static. Time-integrated images of speckle patterns display sharp contrast between bright and dark speckles when the scattering inhomogeneities are not in motion and reduced contrast or blurring when the inhomogeneities are in motion, figure 1.4. In the case of biological tissue blood cells are in motion so the resulting speckle pattern contains information about blood flow.
In order to calculate flow images from raw time-integrated speckle images the blurring caused by motion of reflecting particles is quantified by calculating the speckle contrast (C), defined as the ratio of the standard deviation (σ) to the mean intensity $\langle I \rangle$ for a region of the image:

$$C = \frac{\sigma}{\langle I \rangle} \tag{1.2}$$

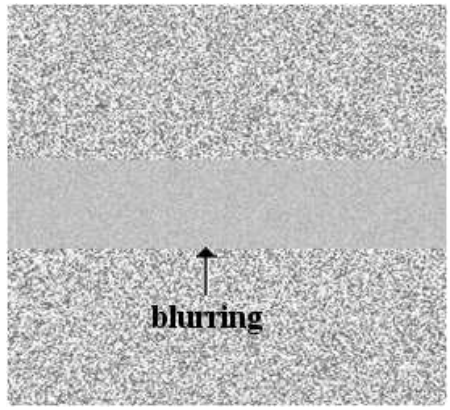

Figure 1.4: Blurring in the speckle pattern.

Larger values of C correspond to lower velocities and vice versa. Ones the image speckle contrast is calculated it is converted into flow images. The most commonly applied technique reported in the literature is a spatial analysis method initially developed by Fercher and Briers [16] for analysing single-exposure speckle photographs. A fundamental disadvantage of this spatial analysis is its temporal resolution. In order to solve this problem, Cheng et. al. [32] proposed a temporal algorithm known as modified Laser Speckle Imaging (mLSI) which has a high spatial resolution but low temporal resolution. mLSI method uses the temporal statistics of the time-integrated speckle. Each pixel in the speckle image can be viewed as the single point area. Then the signal processing consists of calculating the temporal statistics of the intensity of each pixel in the image:

$$N_t = \frac{\langle I^2 \rangle - \langle I \rangle^2}{\langle I \rangle^2} \tag{1.3}$$

where $\langle I^2 \rangle$ and $\langle I \rangle^2$ are the mean and mean-square values of time-integrated speckle intensity variations during the time interval t. Cheng defines $1/Nt$ as the velocity of the scattering particle. Figures $1.5(a)$ and $1.5(b)$ shows the velocity map calculated by the LASCA method and the mLSI method respectively. As we can see there is a significantly improvement in the spatial resolution when the mLSI method is applied.
A fundamental disadvantage of this temporal algorithm is that it does not take account the exposure time of the speckle images which has a impact into the speckle contrast. This issue give us the first aim of this thesis work. In the other hand is well known that there are other effects which determine the speckle contrast, such as the speckle size-pixel ratio. This issue give us the second aim of this thesis work.

1.4 Objectives

1. It is the first aim of this project to include the exposure time into a modified laser speckle imaging method. The challenge is to study the impact of the integration

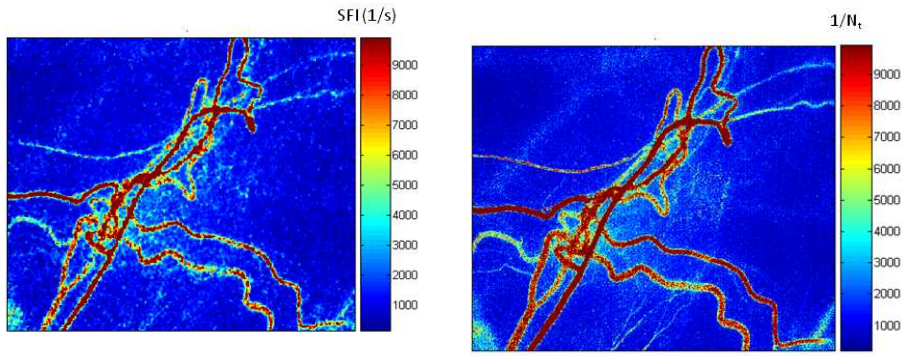

(a) SFI (b) $1/N_t$

Figure 1.5: Velocity map of the laser speckle image of the roedent brain calculated by spatial analisys. Velocity map of the laser speckle image of the roedent brain calculated by temporal analisys [7].

time on the calculations of the speckle flow index.

2. The second aim is study the effect of speckle-pixel size ratio in dynamic speckle contrast and relative flow speed measurement.

1.5 Thesis Overview

Having introduced the main objective of the project, this final section will give an overview of the development of the thesis towards the goal of non-invasive blood flow measurement by LSI.
In Chapter 2 the theory of LSI is discussed in detail, introducing important definitions relevant to the in vivo monitoring of blood flow. The two methods for speckle images analysis are described, with emphasis on the models employed in this project.
Chapter 3 discusses the measurements of blood flow by temporal method using in vitro flow phantom. The need for account the exposure time into a modified laser speckle imaging method is highlighted by calculating the poor agreement between speckle flow index measured with original mLSI method and those obtained by including the exposure time in the mLSI. The feasibility of using mLSI to monitor blood flow is once again addressed.
Chapter 4 discusses the measurement of blood flow by both methods LSI and mLSI. The flow phantom designed for this experiment is described. The potential effects of speckle-pixel size ratio in dynamic speckle contrast and relative flow speed measurement is investigated. The ability of each of these methods to determine the blood flow is assessed.
Chapter 5 discusses the work done in the Ontario Cancer Institute, about Trans-illumination Breast Spectroscopy (TiBS) system for the assessment of breast health. Introduces the

breast cancer disease and its impact on women. It provides information on the methods of detection and presents trans-illumination spectroscopy non-invasive optical methods that are still under research.

Chapter 2

Theory

In this chapter the physics of speckle is reviewed. Develops the maths behind the speckle contrast and connects it to velocity of the scatters. The statistical description of speckle originally developed by Goodman [22] will be used in this thesis work.

2.1 Speckle pattern

When coherent light illuminates a rough surface or passes trough a scattering volume, light is randomly scattered by the roughness or by a great number of inhomogeneities inside the volume. Scattered waves leads to the formation of stochastic spatial distribution of the scattered light intensity which is called speckle pattern.
Skin tissue is a complex biological structure. In a simple representation skin consist in two mayor layers. The outer layer, the epidermis, is typically 40-μm thick, but it can be much thicker on load-bearing areas such as palms and soles, the inner layer called dermis, is between 1 to 4 mm thick and consists mainly of connective tissue composed of collagen fibers. Other dermal structures include nerves, blood vessels, lymph vessels, muscles, and gland units. Figure 2.1 shows what happen to the incident coherent light at the skin. Some of the incident light penetrate into the skin travelling and hitting various physiological particles repeatedly into an scattering process. Some of the scattered light ultimately return to the surface and exit from the skin in various directions creating a speckle patter. This speckle patter will in turn fluctuate in intensity due the motion of the blood cells. Then, as the rate of these intensity fluctuations depends on how fast the blood cells are moving the blood flow could be determinate by processing the fluctuations of the intensity of scattered light. If a statistical analysis of the volume scattered light is performed it is possible calculate the degree of coherence of the light before and after interacting with the tissue. Thus, when performing a coherence correlation, it is possible to calculate the rate of perfusion fluid into the tissue analysed.

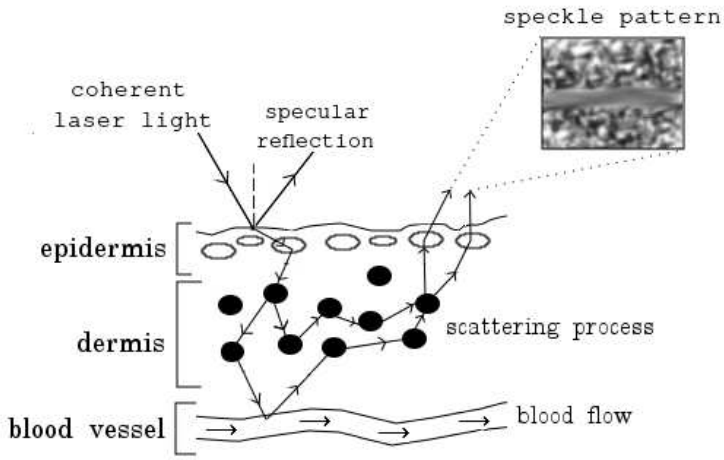

Figure 2.1: Random scattering by tissue components.

2.2 Statistical properties of random light

An arbitrary wave is described by a arbitrary wavefunction ($u(\vec{r},t) = Re\{U(\vec{r},t)\}$) where $U(\vec{r},t)$ is a complex function of time and position which represent the complex field amplitude [18].
For light the functions $u(\vec{r},t) = Re\{U(\vec{r},t)\}$ and $U(\vec{r},t)$ are random and are characterized by their statistical averages.

2.2.1 Optical Intensity

For coherent light the Intensity as a position and time function ($I(\vec{r},t)$) is the absolute square of the complex field amplitude $U(\vec{r},t)$,

$$I(\vec{r},t) = |U(\vec{r},t)|^2 \tag{2.1}$$

For random light, $U(\vec{r},t)$ is a random function of time and position. The intensity $|U(\vec{r},t)|^2$ is therefore also random. The average intensity is then defined as

$$I(\vec{r},t) = \langle |U(\vec{r},t)|^2 \rangle \tag{2.2}$$

where the symbol $\langle \cdot \rangle$ now denotes an ensemble average over many realizations of the random function. For deterministic light, the averaging operation is unnecessary since all trials produce the same wavefunction, so that Eq. 2.2 is equivalent to Eq. 2.1. The average intensity may be time independent or may be a function of time, as illustrated in figures 2.2.
The former case applies when the optical wave is statistically stationary or $I(\vec{r})$; that is, its statistical averages are invariant over time. The instantaneous intensity $|U(\vec{r},t)|^2$ fluctuates randomly with time, but its average is constant. On the other hand, the ran-

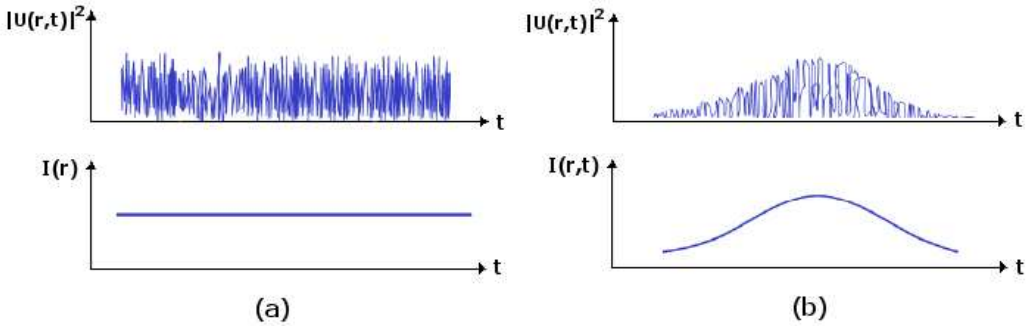

Figure 2.2: Waves statistically stationary (a) and statistically nonstationary (b).[18]

dom intensity $|U(\vec{r},t)|^2$ fluctuates with both position and time, as illustrated in figure 2.2.

A random process is called *ergodic*, if any average calculated along a sample function (i.e., a time average) must equal the same average calculated across the ensemble (i.e., an ensemble average) [20]. For a random process to be ergodic, it is necessary that it be strictly stationary. Thus when light is stationary, the statistical averaging operation in Eq. 2.2 can usually be determined by time averaging over a long time duration instead of averaging over many realizations of the wave as

$$I(\vec{r}) = \lim_{T\to\infty} \frac{1}{2T} \int_{-T}^{T} |U(\vec{r},t)|^2 dt \tag{2.3}$$

2.2.2 Temporal Coherence

First of all consider the fluctuations of stationary light at a fixed position $\vec{r}$ as a function of time $U(t)$ [1] . The function $U(t)$ at two times t, and, $t+\tau$ can in general have different values so that $U(t+\tau)$ $\neq$U(t). Nevertheless when τ is very small compared to times typifying the fluctuation in $U(t)$, $U(t+\tau)$ will be very close to $U(t)$. As τ increases the deviation of $U(t+\tau)$ from $U(t)$ is more likely to be non-zero. Thus in some sense we cans say that the value $U(t+\tau)$ is correlated with $U(t)$ when τ is small but that correlation is lost at τ becomes large compared with the period of the fluctuations. A measure of this correlation is the autocorrelation function of $U(t)$.

Temporal Coherence Function

The autocorrelation function of $U(t)$ is the average of the product of $U^*(t)$ and $U(t+\tau)$ as a function of the time which the degree complex of coherence decrease monotonically (τ) written as [18]

[1] The stationary random function $U(\vec{r},t)$ has a constant intensity $I(\vec{r}) = \langle |U(\vec{r},t)|^2 \rangle$. For simplicity the r dependence will be drop since r is fixed. so that $U(\vec{r},t) = U(t)$ and $I(\vec{r}) = I$, [18]

$$
\begin{aligned}
G(\tau) &= \langle U^*(t)U(t+\tau)\rangle \\
&= \lim_{T\to\infty}\frac{1}{2T}\int_{-T}^{T} U^*(t)U(t+\tau)dt
\end{aligned}
\tag{2.4}
$$

In the phasor picture, $\langle U(t)\rangle = 0$ when the phase of the phasor $U(t)$ is equally likely to have any value between 0 and 2π, as illustrated in figure 2.3.

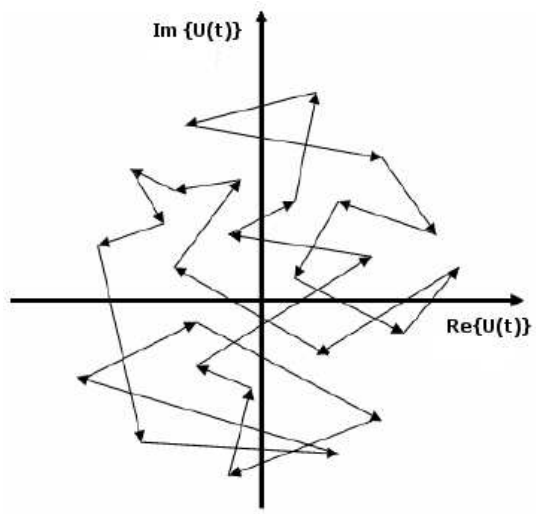

Figure 2.3: Variation of the phasor $U(t)$ with time when its argument is uniformly distributed between 0 and 2π. The average values of its real and imaginary parts are zero, so that $\langle U(t)\rangle = 0$. [18].

- If $U(t)$ and $U(t+\tau)$ are uncorrelated, the autocorrelation $U^*(t)U(t+\tau)$ has a totally uncertain angle, so that it is equally likely to take any direction making its average, the autocorrelation function $G(\tau)$, vanish.
- If, for a given τ, $U(t)$ and $U(t+\tau)$ are correlated, they will maintain some relationship. Their fluctuations are then linked together, so $U^*(t)U(t+\tau)$ has a preferred direction and its average $G(\tau)$ will not vanish.

Therefore when $\tau = 0$, the intensity, defined by Eq. 2.2 is simply $I = G(0)$. The correlation function is known as the *temporal coherence function* in the language of optical coherence theory.

Complex Degree of Coherence

The complex degree of temporal coherence defined [18]

$$g(\tau) = \frac{G(\tau)}{G(0)} = \frac{\langle U^*(t)U(t+\tau)\rangle}{\langle U^*(t)U(t)\rangle} \tag{2.5}$$

It is the normalized autocorrelation function and is insensitive to the intensity. The value of $|g(\tau)|$ is a measure of the degree of correlation between $U(t)$ and $U(t+\tau)$ and its absolute value can not exceed unity

$$0 \leq |g(\tau)| \leq 1 \tag{2.6}$$

However if $|g(\tau)|$ decreases monotonically with τ, at which it drops to a prescribed value serves as a measure of the memory time of the fluctuations known as the coherent light, figure 2.4. Mathematically the coherence time is represent as [18]

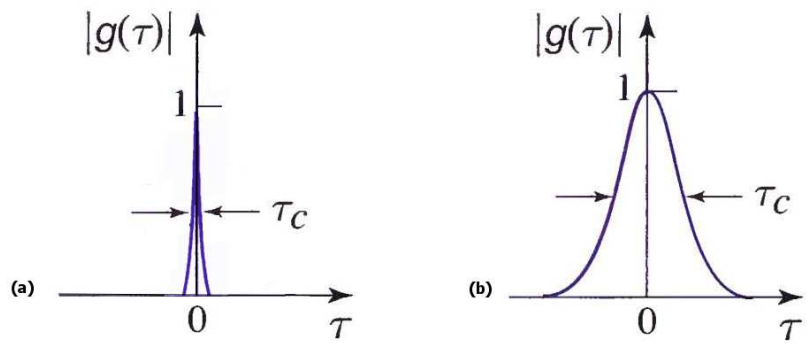

Figure 2.4: Magnitude of the complex degree of temporal coherence $g(\tau)$, and the coherence time τ_c for an optical field with short (left) coherence time and long coherence time (right). [18]

$$\tau_c = \int_{\infty}^{\infty} |g(\tau)|^2 d\tau \tag{2.7}$$

In general, τ_c is the width of the function $|g(\tau)|$ Fig. 2.4. When $\tau < \tau_c$ the fluctuation of the wave are correlated. In the other hand when $\tau > \tau_c$ the fluctuation are uncorrelated.

Mutual Degree of Coherence

The cross-correlation function of $U(\vec{r}_1, t)$ and $U^*(\vec{r}_2, t)$at pairs of positions $\vec{r}_1$ and $\vec{r}_2$, is defined as [18]

$$G(\vec{r}_1, \vec{r}_2, \tau) = \langle U^*(\vec{r}_1, t)U(\vec{r}_2, t+\tau)\rangle \tag{2.8}$$

This function of the time delay τ is known as the *mutual coherence function* and its normalization is called the *complex degree of coherence*.

$$g(\vec{r}_1, \vec{r}_2, \tau) = \frac{G(\vec{r}_1, \vec{r}_2, \tau)}{[I(\vec{r}_1)I(\vec{r}_2)]^{1/2}} \tag{2.9}$$

It is therefore considered a measure of the degree of correlation between the fluctuations at $\vec{r}_1$ and those at $\vec{r}_2$ at a time τ later.
When the two phasors $U(\vec{r}_1)$ and $U(\vec{r}_2)$ fluctuate independently and their phases are totally random $|g(\vec{r}_1, \vec{r}_2, \tau)| = 0$. Light fluctuations at the two points are uncorrelated. The other limit, $|g(\vec{r}_1, \vec{r}_2, \tau)| = 1$, applies when the light fluctuations at $\vec{r}_1$, and at $\vec{r}_2$ a time τ later, are fully correlated.

2.2.3 Spatial Coherence

The mutual coherence function on position for a fixed time delay $\tau = 0$.

$$G(\vec{r}_1, \vec{r}_2) = \langle U^*(\vec{r}_1, t) U(\vec{r}_2, t) \rangle \tag{2.10}$$

is known as the mutual intensity and describes the spatial coherence completely. The complex degree of coherence $g(\vec{r}_1, \vec{r}_2, 0)$ is similarly denoted by $g(\vec{r}_1, \vec{r}_2)$. Thus the complex degree of coherence

$$g(\vec{r}_1, \vec{r}_2) = \frac{G(\vec{r}_1, \vec{r}_2)}{[I(\vec{r}_1) I(\vec{r}_2)]^{1/2}} \tag{2.11}$$

is the normalized mutual intensity. The magnitude $|g(\vec{r}_1, \vec{r}_2)|$ is bounded between zero and is regarded as a measure of the degree of spatial coherence.
The spatial coherence of quasi-monochromatic light in a given plane in the vicinity of a given position $\vec{r}_2$ is described by $|g(\vec{r}_1, \vec{r}_2)|$ as a function of the distance $|\vec{r}_1 - \vec{r}_2)|$. This function is unity when $\vec{r}_1 = \vec{r}_2$ and drops as $|\vec{r}_1 - \vec{r}_2)|$ increases. The area scanned by the point $\vec{r}_1$ within which the function $|g(\vec{r}_1, \vec{r}_2)|$ is greater than some prescribed value is called the coherence area. It represents the spatial extent of $|g(\vec{r}_1, \vec{r}_2)|$ as a function of $\vec{r}_1$ for fixed $\vec{r}_2$, as showed in figure 2.5,

2.3 Random Phasor Sum

A complex addition of N small independent phasors results, for example, when we calculate the total complex amplitude of the wave that arises as a result of scattering by a collection of N small, independent scatterers. Each elementary phasor in this sum is the randomly-phased partial wave scattered from the scattering volume that arrives at the observation point, the resultant phasor amplitude of the field can be represented by

$$U(\vec{r}) = \sum_{k=1}^{N} a_k e^{j\Phi_k} \tag{2.12}$$

where a_k is the random amplitude of the kth elementary random phasor and Φ_k is its random phase, figure (2.6). The statistical properties of (2.12) are determined by the statistical properties of elementary random phasor.

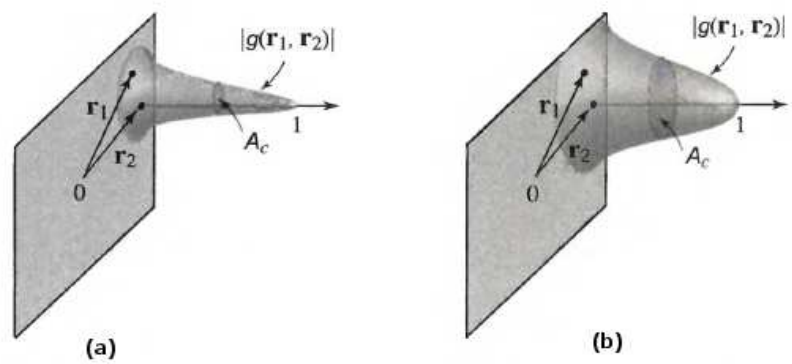

Figure 2.5: Examples of the magnitude of the normalized mutual intensity as a function of $\vec{r}_l$ in the vicinity of a fixed point $\vec{r}_2$. The coherence area in (a) is smaller than that in (b). Bahaa E. A. Saleh, *Fundamentals of Photonics*, Chapter 10. Copyright John Wiley & Sons, Inc. (1991).

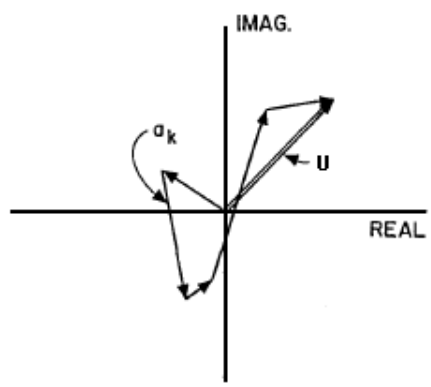

Figure 2.6: Resultant phasor amplitude U.

In order to find the Probability Density Function of the intensity, important assumptions about the contributions from the elementary scatterers are made:

1 The amplitude $|a_k|$ and the phase Φ_k of the kth elementary random phasor is statistically independent of $|a_l|$ and Φ_l for $k \neq l$, that means, knowledge of one phasor's amplitude and/or phase does not imply knowledge of another phasor's amplitude and/or phase and of the amplitudes and phases of all others.

2 The phases Φ_k of the contributions are uniformly distributed on the interval $[-\pi, \pi]$. That is, all values of the phase are equally likely.

In the limit of very large N, the Probability Density Function (PDF) of the real and imaginary parts of the resultant phasor, given by Eq.(2.12) have a large number of independent random variables [20], thus under this circumstances the statistics of the

sum of N independent random varibles are close to Gaussian when $N \to \infty$. The probability density functions for the length a and the phase θ becomes

$$p_{a,\theta}(a,\theta) = \frac{a}{2\pi\sigma^2} e^{\frac{a^2}{2\sigma^2}} \tag{2.13}$$

for $a \geq 0$ and $-\pi \leq \theta < \pi$, otherwise is zero.
From this result the PDF for the length a is

$$p_a(a) = \int_{-\pi}^{\pi} p_{a,\theta}(a,\theta) d\theta = \frac{a}{\sigma^2} e^{\frac{a^2}{2\sigma^2}} \tag{2.14}$$

for $a \geq 0$. This is known as the Rayleigh density function [24].
On the other hand, integrating Eq. 2.13 with respect of a we have

$$p_\theta(\theta) = \frac{1}{2\pi} \tag{2.15}$$

for $-\pi \leq \theta < \pi$. Here it is used that the integral of the Rayleigh density function must be unity.
At the moment, we know the connection between the complex amplitude and the intensity, we can find the probability density function (PDF) for the intensity using the following transformation [26]

$$p_v(v) = p_u(f^{-1}(u)) \left| \frac{du}{dv} \right| \tag{2.16}$$

where $v = I$ and $u = |a| = a$ and

$$I = f(a) = a^2 \tag{2.17}$$

considering a large number of random phasors N which are uniformly distributed on $(-\pi, \pi)$, using the equation 2.16 we can transform the PDF for the phasor length as

$$p_I(I) = \frac{\sqrt{I}}{\sigma^2} e^{\frac{I}{2\sigma^2}} \frac{1}{2\sqrt{I}} = \frac{1}{2\sigma^2} e^{-\frac{I}{2\sigma^2}} \tag{2.18}$$

for $(I \geq 0)$. This result shows that the distribution is a negative exponential. The moments of 2.18 are given as

$$\langle I^n \rangle = \int_0^\infty I^n p_I(I) dI = n!(2\sigma^2)^n \tag{2.19}$$

then the *first moment* of I is

$$\langle I \rangle = 2\sigma^2 \tag{2.20}$$

thus the probability density function of the intensity I is found to be

$$p_I(I) = \frac{1}{\langle I \rangle} e^{-\frac{I}{\langle I \rangle}} \tag{2.21}$$

This function indicates that the phases of the component phasors are uniformly distributed and gives the greatest variation of intensity in the speckle pattern and is called as *fully developed speckle*.
The nesimo moment of the intensity is given by

$$\langle I^n \rangle = n! \langle I \rangle^n \tag{2.22}$$

now the *second moment*, this means n=2 on 2.22, of I is given by

$$\langle I^2 \rangle = 2 \langle I \rangle^2 \tag{2.23}$$

from the second moment, the variance of I

$$\begin{aligned} \sigma_I^2 &= \langle I^2 \rangle - \langle I \rangle^2 \\ \sigma_I^2 &= 2\langle I \rangle^2 - \langle I \rangle^2 \\ \sigma_I^2 &= \langle I \rangle^2 \\ \sigma_I &= \langle I \rangle \end{aligned} \tag{2.24}$$

How much fluctuation of intensity there is compared to the mean intensity is defined as the *speckle contrast* [21].

$$C = \frac{\sigma_I}{\langle I \rangle} \tag{2.25}$$

in fact, from equation 2.24 the contrast for fully developed speckle becomes $C = 1$.
The expression for the contrast of a speckle pattern major importance because it is used as the basic theory that supports the non-invasive technique used to image blood flow called Laser Speckle Contrast Imaging. It was introduced by Fercher and Briers in 1981 [9]. They developed the first speckle model which is based on the first-order spatial statistics of time-integrated speckle. One of the disadvantage of their model did not account for speckle averaging effects. The size of the individual speckles is determined entirely by the aperture of the optical system used to observe the speckle pattern. Next section deals with the speckle size.

2.4 Speckle Size

There are two types of observable speckle, objective speckle and subjective speckle [27]. When the pattern produced by scattered light from scattering media is projected onto a screen where it is observed directly it is called objective speckle pattern. The pupil of the optical detector determines the speckle size, see figure 2.7.
When the scattered light that produce the speckle pattern is projected onto a screen through a lens, the speckle pattern is called subjective. In this case the setting of the aperture stop is who determines the speckle size, see figure 2.8.

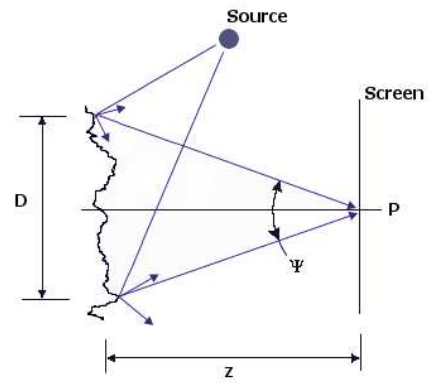

Figure 2.7: Objective speckle set-up

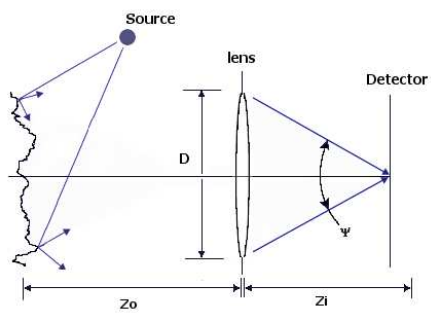

Figure 2.8: Subjective speckle set-up

The laser speckle images for this thesis were obtained with the subjective speckle configuration for this reason is important to calculate the speckle size.
To estimate the speckle size in the image plane of the lens, the distance of which from the lens is z_i, we need only treat the disk enclosed by the pupil of the lens as an uniformly illuminated diffuse surface. If the diameter of the lens pupil is D an analysis of this problem, leads to the expression for the speckle size speckle size (d_{min}),

$$d_{min} = 1.22\lambda \left(\frac{z_i}{D}\right) \tag{2.26}$$

where λ is the wavelengt of the laser light. In the other hand the lens equation

$$\frac{1}{z_o} + \frac{1}{z_i} = \frac{1}{F} \tag{2.27}$$

and the definition of magnification

$$M = \frac{z_i}{z_o} \tag{2.28}$$

combining equations 2.27 and 2.28 the equation 2.26 becomes

$$d_{min} = 1.22\lambda \frac{F(1+M)}{D} \tag{2.29}$$

or more precisely

$$d_{min} = 1.22\lambda(1+M)\#f \tag{2.30}$$

where $\#f$ is the number of the lens.
The speckle size plays a important role in the speckle contrast calculation because it must be included as was demonstrated in [28]. Next section shows how this first model has been improved. The statistics of time-integrated intensity developed by Goodman [20] may be used for this analysis .

2.5 Statistical Properties of Time Integrated Intensity

2.5.1 Integrated Intensity from only Dynamic Scatterers

The variance of time integrated intensity is a simple way to quantify the contrast of the speckle pattern formed at the image. For a given exposure time T each point in the speckle imaging is proportional to the intensity received by the optical detector. Thus time-integrated intensity a that point is [20]

$$W(t) = \int_{t-T}^{t} I(\xi)d\xi \tag{2.31}$$

First of all we have to consider that we are dealing with an ergodic and stationary process. It means that the average over the whole ensemble is the same as the average in time and the statistics of Time-integrated intensity (W) do not depend on the particular observation time t. Then, for simplicity we can write

$$W = \int_{-T/2}^{T/2} I(\xi)d\xi \tag{2.32}$$

2.5.2 Average of Time Integrated Intensity

The mean of W is simply given by

$$\langle W \rangle = \int_{-T/2}^{T/2} \langle I(\xi) \rangle d\xi = T\langle I \rangle \tag{2.33}$$

Now we have to calculate the second moment of W which is given by

$$\langle W^2 \rangle = 2\langle W \rangle^2 \tag{2.34}$$

where

$$
\begin{aligned}
\langle W\rangle^2 &= \left\langle \int_{-T/2}^{T/2} I(\xi)d\xi \right\rangle^2 \\
&= \left\langle \int_{-T/2}^{T/2} I(\xi)d\xi \int_{-T/2}^{T/2} I(\xi^{'})d\xi^{'} \right\rangle \\
&= \int_{-T/2}^{T/2}\int_{-T/2}^{T/2} \left\langle I(\xi)I(\xi^{'})\right\rangle d\xi d\xi^{'} \\
&= \int_{-T/2}^{T/2}\int_{-T/2}^{T/2} \langle G^{(2)}(\xi-\xi^{'})\rangle d\xi d\xi^{'} \qquad (2.35)
\end{aligned}
$$

where Second order of autocorrelation function ($G^{(2)}(\xi-\xi^{'})$) of the autocorrelation intensity $G(\tau)$ and is given by:

$$
G^{(2)}(\xi-\xi^{'}) = \langle I(\xi)I(\xi^{'})\rangle = \langle U(\xi)U(\xi')U^{*}(\xi)U^{*}(\xi')\rangle \qquad (2.36)
$$

where $U(\xi)$ and $U(\xi')$ are the underlying fields. Its normalised form

$$
g^{(2)}((\xi-\xi^{'})) = \frac{\langle I(\xi)I(\xi^{'})\rangle}{\langle I^2\rangle} \qquad (2.37)
$$

The relationship between the second order correlation function (2.37) and the first order correlation function (2.5), is given by

$$
g^{(2)}(\tau) = 1 + \beta|g^{(1)}(\tau)|^2, \qquad (2.38)
$$

where τ is the τ. This is the Siegert relation [29], where β is a normalization factor which accounts for speckle averaging due to mismatch of speckle size and detector size, polarization and coherence effects [30]. Then the second moment (Eq. 2.35) is rewritten as

$$
\langle W^2\rangle = \langle I\rangle^2 \int_{-T/2}^{T/2}\int_{-T/2}^{T/2} \{1+\beta[g^{(1)}(\xi-\xi^{'})]^2\} d\xi d\xi^{'} \qquad (2.39)
$$

2.5.3 Variance of the Time Integrated Intensity

Now we are able to calculate the variance of σ_W^2 as

$$
\begin{aligned}
\sigma_W^2 &= \langle W^2\rangle - \langle W\rangle^2 \\
&= \langle I\rangle^2 \int_{-T/2}^{T/2}\int_{-T/2}^{T/2}\{1+\beta[g^{(1)}(\xi-\xi^{'})]^2\}d\xi d\xi^{'} - T^2\langle I\rangle^2 \\
&= \langle I\rangle^2 \left[\int_{-T/2}^{T/2}\int_{-T/2}^{T/2} d\xi d\xi^{'} + \int_{-T/2}^{T/2}\int_{-T/2}^{T/2}\beta[g^{(1)}(\xi-\xi^{'})]^2\}d\xi d\xi^{'}\right] - T^2\langle I\rangle^2 \\
&= \langle I\rangle^2 T^2 + \langle I\rangle^2 \int_{-T/2}^{T/2}\int_{-T/2}\beta[g^{(1)}(\xi-\xi^{'})]^2\}d\xi d\xi^{'} - T^2\langle I\rangle^2 \\
&= \langle I\rangle^2 \int_{-T/2}^{T/2}\int_{-T/2}^{T/2}\beta[g^{(1)}(\xi-\xi^{'})]^2 d\xi d\xi^{'} \qquad (2.40)
\end{aligned}
$$

were $g^{(1)}(\xi-\xi^{'})$ represents the autocorrelation function of the instantaneous intensity. Since the integrand is an even function of $(\xi,\xi^{'})$, the double integral can be reduced to a single integral. Thus we have

$$
\sigma_W^2 = \langle I\rangle^2 \left[\frac{1}{T}\int_{-\infty}^{\infty}\Lambda\left(\frac{\tau}{T}\right) g^{(1)}(\tau)d\tau\right] \qquad (2.41)
$$

where $\tau(\xi,\xi^{'})$ and

$$
\Lambda(\tau) \equiv \begin{cases} 1-|\tau| & |\tau|\leq 1 \\ 0 & \text{otherwise} \end{cases}
$$

Assuming that the velocity of the scatterers have a Lorentzian distribution [20], which gives $g_f^{(1)}(t) = e^{-t/\tau_c}$, then the contrast is given by [28]

$$
\begin{aligned}
K &= \frac{\sigma_W}{\langle I\rangle} \\
&= \left(\beta\frac{\tau_c}{T} - \frac{\tau_c^2}{2T}(e^{-2T/\tau_c}-1)\right)^{1/2} \qquad (2.42) \\
&= \left(\beta\frac{e^{-2x}-1+2x}{2x^2}\right)^{1/2}
\end{aligned}
$$

where $x = \frac{T}{\tau_c}$ and τ_c is the correlation time of the light scattered by the sample.
Eq. 2.42 is valid for light scattered from blood cell which moves trough blood vessels. Next section discusses about light scattered from the surrounding tissue that remains static.

2.5.4 Integrated intensity from Static and Dynamic Scatterers

When the subject under study has static and dynamic scattering components, is a non-ergodic process [31] the Siegert relation cannot be applied, this represent a problem

when measuring the temporal intensity correlation function $g^{(2)}(\tau)$ but is not a problem if one is measuring the temporal field correlation function $g^{(1)}(\tau)$ directly [31].
The speckle patter intensity is actually a superposition of photons from static region on the biological sample represented by $U_c(t)$ and dynamic or fluctuating component represented as $U_f(t)$, that means that the total electric field is actually the sum,

$$U(t) = U_c(t) + U_f(t) \tag{2.43}$$

so the correlation function

$$\begin{aligned} g^{(1)}(\tau) &= \frac{\langle U(t)U^*(t+\tau)\rangle_t}{\langle |U|^2\rangle} \\ &= \frac{\langle U_c(t)U_c^*(t+\tau)\rangle_t + \langle U_f(t)U_f^*(t+\tau)\rangle_t}{I_c + \langle I_f\rangle + \langle U_c(t)U_f^*(t)\rangle_t + \langle U_f(t)U_c^*(t)\rangle_t} \\ &+ \frac{\langle U_c(t)U_f^*(t+\tau)\rangle_t + \langle U_f(t)U_c^*(t+\tau)\rangle_t}{I_c + \langle I_f\rangle + \langle U_c(t)U_f^*(t)\rangle_t + \langle U_f(t)U_c^*(t)\rangle_t} \end{aligned} \tag{2.44}$$

where $I_c = \langle U_c(t)U_c^*(t+\tau)\rangle_t$ and $\langle I_f\rangle = \langle U_f(t)U_f^*(t+\tau)\rangle_t$, because constant and fluctuating are uncorrelated third and fourth term in the denominator of line one of (2.44) are zero, is the same thing with the entire second line. We can recognize that $G_f^{(1)}(\tau) = \langle U_f(t)U_f^*(t+\tau)\rangle_t$. Thus $g^{(1)}(\tau)$ becomes

$$g^{(1)}(\tau) = \left[\frac{I_c + \langle I_f\rangle g_f^{(1)}(\tau)}{I_c + \langle I_f\rangle}\right]^2 \tag{2.45}$$

then

$$[g^{(1)}(\tau)]^2 = \frac{I_c^2 + 2I_c\langle I_f\rangle g_f^{(1)}(\tau) + \langle I_f\rangle^2 (g_f^{(1)})^2(\tau)}{(I_c + \langle I_f\rangle)^2} \tag{2.46}$$

lets call $A = \langle I_f\rangle/\langle I_f\rangle + I_c$ and $B = I_c/I_c + \langle I_f\rangle$, moreover $A + B = 1$, renaming $\rho = A = B - 1$ then we can write

$$[g^{(1)})(\tau)]^2 = (1-\rho)^2 + 2\rho(1-\rho)[g_f^{(1)}(\tau)] + A^2[g_f^{(1)})(\tau)]^2 \tag{2.47}$$

substituting (2.47) into (2.41) we have

$$\begin{aligned} \sigma_W^2 &= \langle I\rangle^2 \left[\frac{1}{T}\int_{-\infty}^{\infty} \beta(1-\rho)d\tau \right. \\ &+ \frac{1}{T}\beta(2\rho(1-\rho))\int_{-\infty}^{\infty} \Lambda\left(\frac{\tau}{T}\right) g_f^{(1)}(\tau)d\tau \\ &+ \left. \frac{1}{T}\beta(\rho^2)\int_{-\infty}^{\infty} \Lambda\left(\frac{\tau}{T}\right)[g_f^{(1)}(\tau)]^2 d\tau\right] \end{aligned} \tag{2.48}$$

where $\tau = (\xi, \xi')$ and

$$\Lambda(\tau) \equiv \begin{cases} 1 - |\tau| & |\tau| \leq 1 \\ 0 & \text{otherwise} \end{cases}$$

So we can rewrite (2.48) as

$$\begin{aligned} \sigma_W &= \langle I \rangle \left[\frac{1}{T} \int_0^T \beta(1-\rho) d\tau \right. \\ &+ \frac{1}{T} \beta(2\rho(1-\rho)) \int_0^T \left(1 - \frac{\tau}{T}\right) [g_f^{(1)}(\tau)] d\tau \\ &+ \left. \frac{1}{T} \beta(\rho^2) \int_0^T \left(1 - \frac{\tau}{T}\right) [g_f^{(1)}(\tau)]^2 d\tau \right]^{1/2} \end{aligned} \tag{2.49}$$

Assuming that the velocity of the scatterers have a Lorentzian distribution [20], which gives $g_f^{(1)}(t) = e^{-t/\tau_c}$
then the contras is given by [30]

$$\begin{aligned} K &= \frac{\sigma_W}{\langle I \rangle} \\ &= \left[\beta(1-\rho)^2 + 4\beta\rho(1-\rho) \left(\frac{\tau_c}{T} - \frac{\tau_c^2}{T^2}(e^{-T/\tau_c} - 1) \right) \right. \\ &- \left. \beta\rho^2 \left(\frac{\tau_c}{T} - \frac{\tau_c^2}{2T}(e^{-2T/\tau_c} - 1) \right) \right]^{1/2} \\ &= \left[\beta(1-\rho)^2 + 4\beta\rho(1-\rho) \frac{e^{-x} - 1 + x}{x^2} + \beta\rho^2 \frac{e^{-2x} + 1 - 2x}{2x^2} \right]^{1/2} \end{aligned} \tag{2.50}$$

where $x = \frac{T}{\tau_c}$ and τ_c is the correlation time of the light scattered by the sample. A practical speckle model that accounts for the presence of static scattered light is given by equation (2.50).
LSI is a method of image analysis based on the spatial statistics of the time-integrated intensity or equation 2.50. However this method has the disadvantage of loss of resolution caused by the need to average over a block of pixels to obtain the spatial statistics (section 2.8). In 2003 Cheng [32] introduces a new method to analyse the LSI based on the temporal statistics of time-integrated intensity which was called modified LSI (mLSI). Next section discuses the theory for such model.

2.6 Multiple Speckle Patterns

Temporal statistic of the time-integrated intensity is used in order to analyse the speckle images [32]. In this case the sums of fully developed speckle patterns will be developed. For N independent speckle patters the total intensity is

$$I_s = \sum_{n=1}^{N} I_n \tag{2.51}$$

where I_s represents the total intensity integrated in certain interval of time T. Analogously, from equation 2.21 the probability density function for one pattern is [23]

$$p_I(I) = \frac{1}{\langle I \rangle} e^{-\frac{I}{\langle I \rangle}} \tag{2.52}$$

The characteristic function for this PDF is given by [23]

$$\begin{aligned} M(w) &= \int_0^\infty e^{jwI} P_I dI \\ &= \int_0^\infty e^{jwI} \left[\frac{1}{\langle I \rangle} e^{-I/\langle I \rangle} \right] dI \\ &= \frac{1}{jw\langle I \rangle} \end{aligned} \tag{2.53}$$

Then the sum of two uncorrelated patterns is

$$\begin{aligned} I_s &= I_1 + I_2 \\ p_{I_1}(I_1) &= \frac{1}{\langle I_1 \rangle} e^{-\frac{I_1}{\langle I_1 \rangle}} \\ p_{I_2}(I_2) &= \frac{1}{\langle I_2 \rangle} e^{-\frac{I_2}{\langle I_2 \rangle}} \end{aligned}$$

where the s refers to the sum.
The characteristic function of the sum of two independent random variables is the product of the characteristic function components [23]

$$M_s = M_1 M_2 \tag{2.54}$$

where

$$\begin{aligned} M_1 &= \frac{1}{jw\langle I_1 \rangle} \\ M_2 &= \frac{1}{jw\langle I_2 \rangle} \end{aligned}$$

then

$$M_s = \frac{1}{jw\langle I_1 \rangle} \frac{1}{jw\langle I_2 \rangle} \tag{2.55}$$

From Eq. 2.51 for N uncorrelated speckle patterns, the characteristic function

$$\begin{aligned} M_s(w) &= \prod_{n=1}^{N} M_n(w) \\ &= \prod_{n=1}^{N} \frac{1}{jw\langle I_n\rangle} \end{aligned} \tag{2.56}$$

The PDF of 2.56 is given by the inverse Fourier transform as [23]

$$p(I_s) = \frac{1}{2\pi}\int_{-\infty}^{\infty} \frac{e^{-jwI_T}}{\prod_n (1 - jw\langle I_n\rangle)} dw \tag{2.57}$$

Assuming that N independent speckles are detected in the time interval T and that the intensity of each of these speckles holds the same weight in a statistical sense, then $n \simeq n_0$, and the intensity is I_0 [25]. With this approximation the probability density function of N speckle patterns becomes

$$p_s(I_s) = \frac{N^N}{\langle I^N\rangle}\frac{I_s^{N-1}}{\Gamma(N)} e^{-NI_s/\langle I\rangle} dw \tag{2.58}$$

where $\langle I\rangle$ is the total average intensity and $\Gamma(N)$ is the gamma function of N.
The Eq. 2.58 is a Gamma distribution from which we can calculate its $k^{(th)}$ moment by

$$\langle I^k\rangle = \frac{(N+k-1)...N}{(N/I)^k} \tag{2.59}$$

First moment of 2.58 is

$$\langle I_s\rangle = \frac{N}{N/\langle I\rangle} = \langle I\rangle \tag{2.60}$$

The second moment

$$\langle I_s^2\rangle = \frac{(N+1)N}{(N/\langle I\rangle)^2} = \langle I\rangle^2 + \frac{\langle I\rangle^2}{N} \tag{2.61}$$

Then the variance is given by

$$\begin{aligned} \sigma_s^2 &= \langle I_T^2\rangle - \langle I_T\rangle^2 \\ &= \langle I\rangle^2 + \frac{\langle I\rangle^2}{N} - \langle I\rangle^2 \\ &= \frac{\langle I\rangle^2}{N} \end{aligned} \tag{2.62}$$

finally

$$N = \frac{\langle I\rangle^2}{\sigma_s^2} \tag{2.63}$$

The equation 2.63 was used for the modified LSI as the factor N_t, indicating that t refers a temporal analysis, by Cheng to measure blood flow dynamics [32] (see 2.8.2).

2.7 Velocity of the Scatters

As we pointed out in the introduction, biological tissue is a scattering media which may contain capillaries, venous and the surrounding tissue. Particles such as blood cells in capillaries are in motion, a speckle pattern from such scattering media fluctuates in time, whereas from surrounding tissue the reflecting particles are static and the speckle pattern remains static. Time-integrated images of speckle patterns display sharp contrast between bright and dark speckles when the scattered light is not in motion and reduced contrast (or blurring) when the scatters are in motion. When laser light illuminates living tissue, the mainly reflecting particles are the blood cells so the resulting speckle pattern contains information about blood flow. One of the models to measure the velocity of the scatters is described,

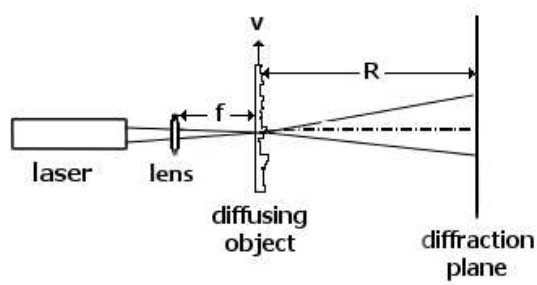

Figure 2.9: Optical system to produce speckle pattern from a diffuse object.

Consider the figure 2.9, the light amplitude of speckle patterns at time t at the far-field plane, a distance R away from the diffuse object, is given by [34]

$$I(\vec{x},t) = \int_{-\infty}^{\infty} exp\left\{-\frac{|u|^2}{w^2} + i\phi(\vec{u}-\vec{v}t)\right\} exp\left(-\frac{2\pi i}{\lambda R}\vec{u}\vec{x}\right) d\vec{u} \tag{2.64}$$

where w is the radius of the illuminating beam with wavelength λ at the object plane, $\phi(u)$ is a random phase of the diffuse object at the co-ordinate vector $\vec{u}$ and $\vec{v}$ is the velocity vector of the moving diffuse object.
If the amplitude $I(\vec{x},t)$ of speckles varying in time obeys a complex Gaussian process, section 2.3, the time autocorrelation of variations of the speckle intensity at the far-field plane is characterized by a normalized absolute square of the second order correlation of $I(x,t)$:

$$g^{(2)}(\vec{r},t-t') = \frac{|\langle I(\vec{r},t)I(\vec{r},t')\rangle|^2}{|\langle |I(\vec{r},t)|^2\rangle|^2} \tag{2.65}$$

By substituting equation 2.64, into equation 2.65, it may be approximately expressed by

$$\langle exp\{i\phi(\vec{u}_1 - \vec{v}t) - i\phi(\vec{u}_2 - \vec{v}t^{'})\}\rangle = \delta(\vec{u}_1 - \vec{u}_2 - \vec{v}\tau_c) \tag{2.66}$$

where $\tau_c = (t - t^{'})$ and $\delta(\vec{u})$ is a delta function. The Fourier transform of 2.66 give us the normalized autocorrelation function $g^{(2)}(\tau)$ as

$$g^{(2)}(\tau) = exp\left(-\frac{v^2\tau_c^2}{w^2}\right) \tag{2.67}$$

where the replacement of $v = |v|$ is taken. The time correlation length of speckle intensity variations at the far-field plane due to the moving diffuse object with constant velocity v may be defined by

$$\tau_c = \frac{w}{v} \tag{2.68}$$

This result shows that the correlation time is determined by the mean velocity which the diffuser moves and is connected with the waist of the laser beam as well [34, 35]. The relationship between τ_c and the mean velocity is not well know [36]. However, as we pointed out in section $2.2.2$ and from 2.68,the mean velocity of the scatters is closely related to autocorrelation function of the intensity. Now it becomes clear that the mean flow velocity determinates the behaviour of the temporal intensity correlation. Therefore the equation 2.68 can be used for measuring the speed of the flow.

2.8 Methods for Laser Speckle Contrast Analysis

Laser speckle imaging (LSI) is one of the techniques to measure blood flow, it was introduced by Fercher and Briers [9] to measure the retinal blood flow. They introduced a single-exposure speckle photography to produce a map of flow velocities based on high-pass spatial filtering technique by mapped as a variation of in the contrast of speckle pattern converting the contrast variation to intensity variations. In 1994 Webster and Briers developed a digital technique that totally eliminates the photographic stage [16]. Detector requires certain exposure time to record the speckle images. If the correlation time of the scattered light, defined by equation 2.36, is less than the exposure time of the camera the changes of the intensity are averaged resulting in a averaged intensity (integrated) in the detector. In addition, due the fluctuations of the blood cells are random we can use the theory developed in the section 2.5 to analyse speckle images and get information about the flow inside of blood vessels. Next sections present the actual methods to performance the LSI images.

2.8.1 Spatial Analysis of Laser Speckle Images

In 2008 Parthasarathy et al. proposed a rigorous and practical robust speckle model that accounts for the presence of static scattered light in this case the contras is defined as [30]

$$K = \left[\beta(1-\rho)^2 + 4\beta\rho(1-\rho)\frac{e^{-x}-1+x}{x^2} + \beta\rho^2\frac{e^{-2x}+1-2x}{2x^2}\right]^{1/2}$$

where $\rho = \langle I_f \rangle / (\langle I_f \rangle + I_c)$. Speckle images are recorded by a CCD camera. In order to measure the contras of those speckle images N_sxN_s pixels windows are employed figure 2.10 a), typically $N_s = \{5, 7\}$. The contrast for the spatial statistics of time-integration speckle image is calculated by using the equation

$$K = \frac{\sigma}{\langle I \rangle} = \frac{\sqrt{\langle I^2 \rangle - \langle I \rangle}^2}{\langle I \rangle} \tag{2.69}$$

The contrast value K is storage into a new image, figure 2.10 b). The pixels window moves forward one pixel and the contrast is calculated again at this new position, this two steps repeat over the speckle image until cover the whole image then a new image is a contras image 2.10 b).

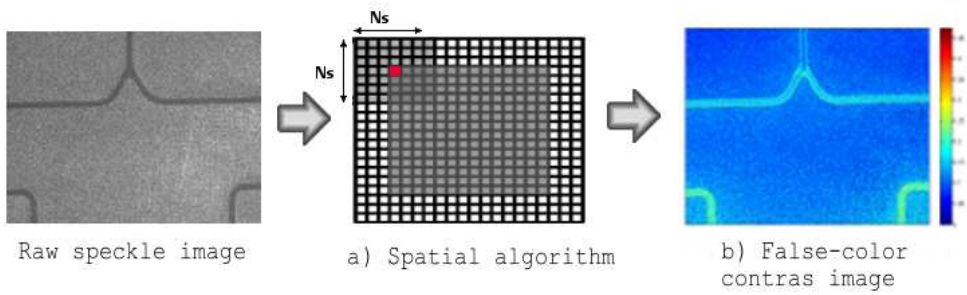

Figure 2.10: Spatial statistics of a time-integrated speckle.

Finally in order to get a measure of the blood flow the equation 2.69 is employed. The contrast values are converted into a *Speckle Flow Index* (SFI) defined as

$$SFI = \frac{1}{\tau_c} \propto bloodflow \tag{2.70}$$

which can be obtained from 2.69 and 2.69 unfortunately there is no way to get $1/\tau_c$ by analytical methods so it is necessary to do the approximation $T \ll \tau_c$ [37]. Then the SFI can be obtained directly from 2.69.

2.8.2 Temporal Analysis of Laser Speckle Images

In 2003 Cheng [32] presented a modified analysis for laser speckle imaging (mLSI) that is based on the temporal statistics of a time-integrated speckle to get the velocity map directly, figure 2.11 b). In this method each pixel in the speckle image can be viewed as the single point area, figure 2.11. Then the signal processing consists of calculating

the temporal statistics of the intensity of each pixel in the image figure 2.11 a) by using the equation

$$1/N_t = \frac{\langle I \rangle^2}{\langle I^2 \rangle - \langle I \rangle^2} \tag{2.71}$$

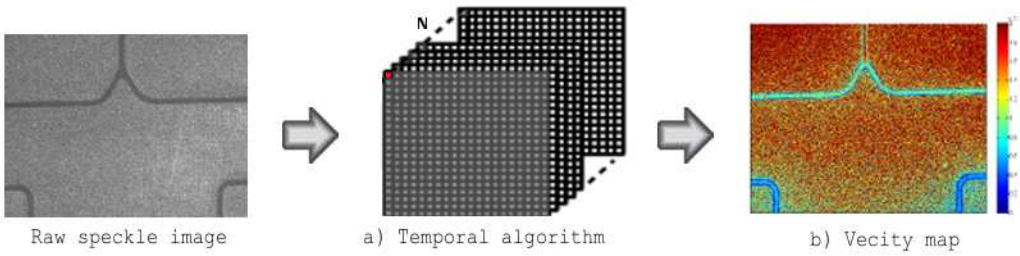

Figure 2.11: Temporal statistics of a time-integrated speckle.

In this thesis we will use both two methods to analyse the speckle images.

2.9 LSI versus mLSI

Up to now the methods for speckle images analysis have been explained by using the two methods. In one hand the spatial method has a disadvantage, the resolution of the technique is limited by the necessary use of a finite number of pixels in computing the local contrast. Lower numbers reduce the validity of the statistics, whereas higher numbers limit the spatial resolution of the technique. In the other hand temporal method requires a certain numbers of speckle images which are limited by the the speed at which the frames are capture, compromising the temporal resolution. Cheng [7] shown that the number of frames should be more than 15 to keep the linearity between N_t and the velocity of the scatters.
Although LSI and mLSI have disadvantages they are methods to get, in a way, measures of blood flow faster than other techniques such as laser Doppler flowmetry (LDf). LSI and mLSI are not a scanning technique and the images acquisition is instantaneously LSI and mLSI are in advantage over LDF.

Chapter 3

Integration of Image Exposure Time into a Modified Laser Speckle Imaging Method

As we mentioned in section 2, the spatial speckle contrast analysis has lost in spatial resolution. To address this issue Cheng [32] developed a modified LSI (mLSI) which preserves the original spatial resolution by sacrificing temporal resolution. A fundamental disadvantage of mLSI is that it does not take into account the camera exposure time. Since the camera exposure time play a fundamental role for monitoring blood flow [38], this chapter deals with incorporate the exposure time into mLSI equation (2.71) and provide experimental support of our approach with measurements from an *in vitro* flow phantom.

3.1 Theory

In section 2.8.2 was shown that mLSI analysis method is based on equation

$$\frac{1}{N_t} = \frac{\langle I \rangle^2}{\langle I^2 \rangle - \langle I \rangle^2} \tag{3.1}$$

where $\langle I \rangle$ and $\langle I^2 \rangle$ are the mean and mean-square values, respectively, of time integrated speckle intensities during the time interval t and for a specific pixel.
from 2 we can show that equation 3.1 is equal to the contrast equation 2.25

$$\frac{1}{N_t} = \frac{1}{K_t^2} \tag{3.2}$$

where K_t is the temporal contrast. For the Lorentzian spectrum approximation [20], it shows that:

$$\frac{1}{K_t^2} \equiv \frac{\langle I \rangle^2}{\langle I^2 \rangle - \langle I \rangle^2} = \left\{ \frac{\tau_c}{T} + \frac{1}{2} \left(\frac{\tau_c}{T} \right)^2 \left[e^{-2(T/\tau_c)} - 1 \right] \right\}^{-1} \tag{3.3}$$

or

$$\frac{1}{K_t^2} = \left\{ \frac{\tau_c}{T} + \frac{1}{2}\left(\frac{\tau_c}{T}\right)^2 [e^{-2(T/\tau_c)} - 1] \right\}^{-1} \tag{3.4}$$

where $\langle I \rangle$ and $\langle I^2 \rangle$ are the mean and mean-square values, respectively. For $T \gg \tau_c$ the equation 3.4 becomes

$$\frac{1}{N_t} = \frac{T}{\tau_c} \tag{3.5}$$

From equation 3.5, it is clear that the physical meaning of the parameter $1/N_t$ is the number of coherence intervals captured during the exposure time T. However, there are multiple combinations of velocity and T that yield the same value of $1/N_t$. Also from equation 3.5, the physical meaning of the speckle flow index $(SFI \equiv 1/\tau_c)$ is the rate of coherence intervals captured over unit time:

$$SFI \equiv \frac{1}{\tau_c} = \frac{1}{TN_t} \tag{3.6}$$

Equation 3.6 is similar to equation 3.2, with the important difference that it accounts for image exposure time so that the target range of velocity sensitivity can be varied.
A large dynamic range would be necessary to study blood flow dynamics in vessels of different type, as well as in response to flow-modulating stimuli (i.e. photocoagulation, vasoactive drugs, etc).
In 2005 Yuan [39] defined the sensivity of LSI to relative changes in flow rate, as the ratio of the relative speckle contrast change to the relative flow speed change as:

$$S_r = \left| \frac{\frac{dK}{K}}{\frac{dv}{v}} \right| = -\frac{\frac{dK}{K}}{\frac{dv}{v}} = -\frac{r}{K}\frac{dK}{r} = \frac{1}{2K^2r^2}[r - 1 + (r+1)e^{-2r}] \tag{3.7}$$

where K is the speckle contrast given by

$$K = \left[\frac{1}{r} + \frac{1}{2}\left(\frac{1}{r^2}\right)(e^{-2r} - 1) \right]^{1/2} \tag{3.8}$$

and $r = T/\tau_c$ is the number of coherent intervals captured per unit time $(i.e., 1/N_t)$. Figure 3.1, we can see that S_r reaches an asymptotic value of 0.5 for values of r greater than ~ 50. Hence, for $r > 50$, the relative speckle contrast response is proportional to the actual relative change in flow speed [39]. Our experimental data 3.3 support this statement, as we observe that a linear response range is achieved for $r = 1/N_t > 50$.
Hence, to determine the optimal image exposure time to use in analysis of relative flow rate changes assessed with LSI, the end-user should calculate relative flow rate changes only if the data sets satisfy the $r > 50$ criterion. This *rule-of-thumb* applies to both mLSI and spatial LSI data. Our experimental data (see Results section below) support this *rule-of-thumb*.

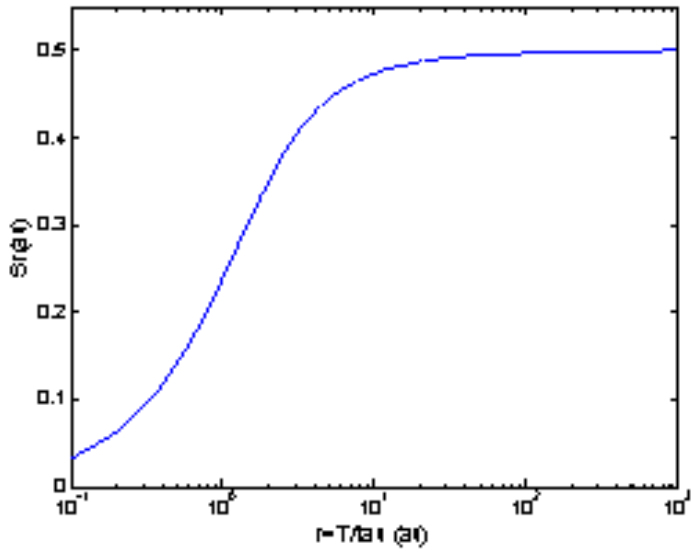

Figure 3.1: Sensitivity as function of the number of coherence intervals captured over unit of time $(i.e., 1/N_t)$.

For an image in which multiple flow speeds are encountered (i.e., microvasculature in a cranial or dorsal window chamber preparation), ideally one would collect sequences of images at multiple exposure times and, with analysis of the ensuing $1/N_t$ maps identify the optimal exposure-time images to use to analyse relative blood flow changes for each pixel. In many experimental scenarios for which high temporal resolution is not required (i.e., cortical spreading depression following focal cerebral ischemia), this approach is viable.

3.2 Experimental design

3.2.1 LSI instrument

The instrument consisted of a $30 - mW$, $633 - nm$ He-Ne laser, plano-convex lens, beam steering mirrors, digital charge-coupled device (CCD) camera equipped with a macro lens, and desktop Personal Computer (PC), figure 3.2. Collimated light emitted from the laser became divergent after passing through the plano-convex lens. To make the instrument more compact, mirrors were used to steer the diverging beam to the target plane. The resultant speckle pattern was imaged on the CCD array at 1:1 magnification and acquired to the PC memory.
The $f - stop$ of the camera lens was set to achieve a sampling rate of two pixels per minimum speckle size [41].

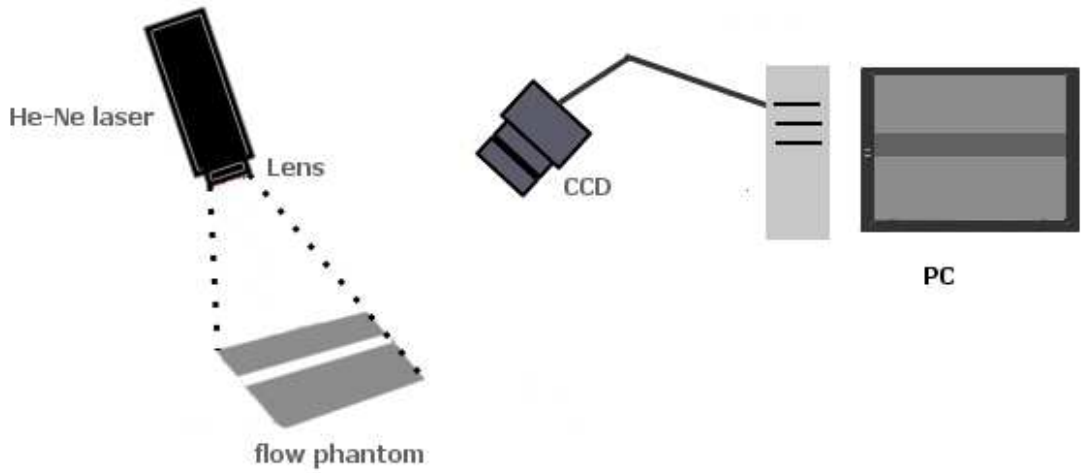

Figure 3.2: Simple representation of the experimental setup employed in this experiment.

3.2.2 In vitro flow phantom

To generate scattering agar gels, we boiled a solution consisting of 100 mL of deionized water and 10 mL of glycerol. The latter was used to improve the mechanical integrity of the resultant gels. We added simultaneously $0.3g$ of $TiO2$ and $2g$ of agar to the boiling solution. The former was used to increase the scattering coefficient of the otherwise clear gels, and the agar added was deemed appropriate to simulate the reduced scattering coefficient of skin. The solution was then poured into various molds (e.g., Petri dishes, sandwiched glass slides) to achieve the desired thickness ($150\mu m$ to several millimeters) and allowed sufficient time to solidify. In specific gels, a $550 - \mu m$ inner-diameter glass capillary tube was embedded into the mold prior to solidification. A syringe-based infusion pump was used to inject fluid into the flow tube. Tygon tubing delivered the fluid from the filled syringe mounted on the pump to the tube embedded in the gel. Intralipid (1%concentration) was used as the fluid in this study.

3.2.3 Experiments

The infusion pump was set to achieve flow rates of up to $13mm/s$. The flow phantom was imaged with the LSI instrument. Image exposure times of 0.1, 1 and $10ms$ were selected as representative values based on those used in previous studies [38, 40, 39].

3.2.4 mLSI image analysis

The mLSI algorithm has been described previously in detail in previous chapter according to [32]. Briefly, the value N_t of each pixel in m consecutive images of the raw speckle pattern was computed according to equation 3.1. Data were rendered as two-

dimensional false-color coded maps which displayed the spatial variation of the flow speed distribution in the region of interest.

3.3 Results

The primary objectives of this manuscript are to illustrate the need to include the image exposure time in mLSI 3.1 and to validate the resultant speckle imaging equation 3.6. To this end, we developed two sets of in vitro flow experiments employing the experimental setup described above.

3.3.1 Camera exposure time needs to be considered with mLSI analysis

In the first set of experiments, we varied the actual flow rate between 1 and $13mm/s$. For these experiments, image exposure time was held constant at $T = 1ms$. To calculate values for mean SFI and $1/N_t$ as a function of the actual flow rate, we selected a $300x100$ subregion of pixels within the tube and calculated the corresponding mean values for each actual flow rate values and the standard deviation of the mean values. A linear relationship between values of SFI and flow rates between 5 and $13mm/s$ was observed figure $3.3(a)$, indicating that $T = 1ms$ is an appropriate exposure time for this range of flow rates. However, for flow rates below $5mm/s$, SFI values deviated from the linear fit, suggesting that $T = 1ms$ was too short to maintain the linear relationship. In a subsequent set of experiments, we varied the actual flow rate between 0.5 and $6mm/s$, with an image exposure time of $T = 10ms$. A longer exposure time was used to shift the linear response range of LSI to slower flow rates [38]. We observed a linear relationship for both parameters (SFI) and $(1/N_t)$, suggesting that $T = 10ms$ is appropriate to maintain a linear response over this range of flow rates figure $3.3(b)$.
From the physical meaning of the parameter $1/N_t$, multiple combinations of T and actual flow rate can produce the same $1/N_t$ value figure $3.4(a)$. For example, consider a $1/N_t$ value of 100. Based on the data in figure 3.3, it is clear that this value will map to different actual flow rate values, depending on which image exposure time is used. Specifically, this value corresponds to either $11mm/s$ ($T = 1ms$, figure $3.3(a)$) or $0.8mm/s$ ($T = 10ms$, figure $3.3(b)$). In contrast, the SFI value is unaffected by a change in exposure time figure $3.4(b)$.
Collectively, these data demonstrate that the linear response range of $1/N_t$ values obtained with the mLSI method, is affected by the image exposure time. This result is in agreement with previous findings [43] and justifies the need to include the image exposure time in the mLSI imaging equation 3.1 and to validate the resultant imaging equation 3.5.

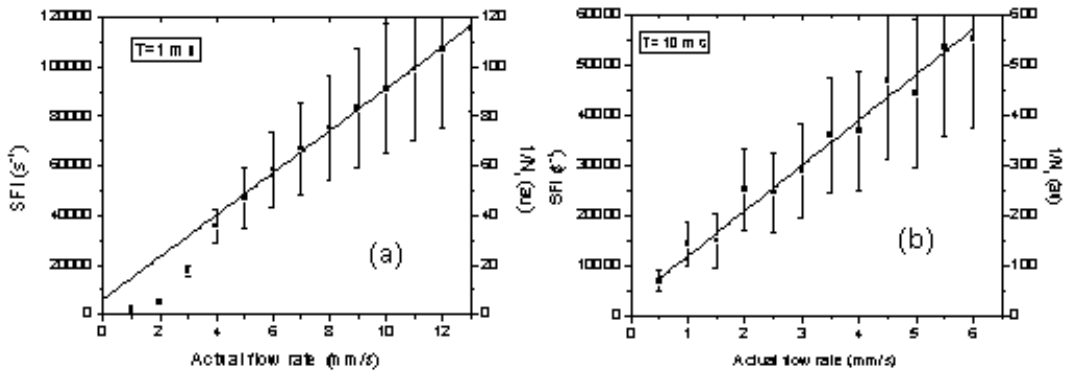

Figure 3.3: (a) Both SFI and $1/N_t$ values maintain a linear relationship to the actual flow rate, for an actual flow rate greater than $5mm/s$ and image exposure time of $1ms$. For an actual flow rate less than $5mm/s$, it is necessary to employ a longer exposure time to achieve a linear response, as demonstrated in (b) for $T = 10ms$.

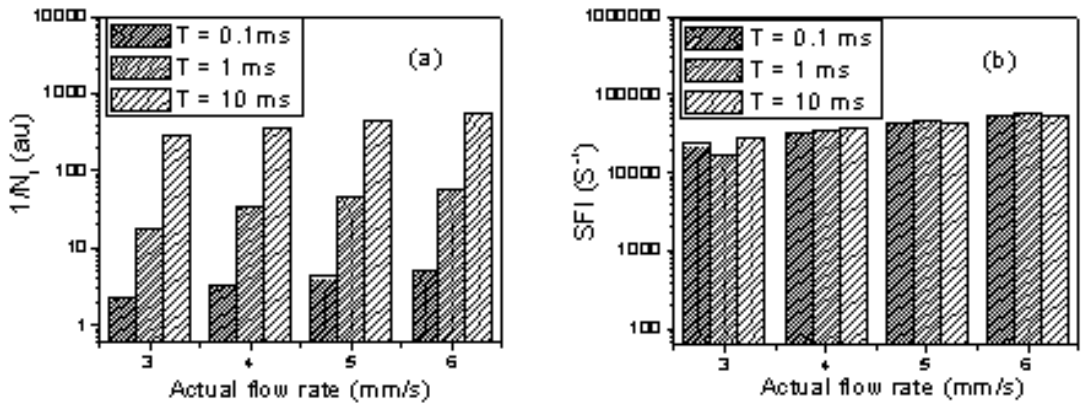

Figure 3.4: (a) $1/N_t$ and (b) SFI values as a function of the actual velocity, for four exposure times (T). Note that, for a given actual flow rate, the $1/N_t$ value depends on exposure time, while the SFI value is unaffected.

3.3.2 Incorporation of the exposure time in the mLSI model improves substantially the accuracy of this method to measure relative flow rate changes.

We now calculate the relative flow rate change predicted with the mLSI model $[1/N_t$, equation 3.1] and our proposed model $[SFI$, equation 3.6]. To do this, we acquired speckle flow images from the above-described in vitro flow phantom at two actual flow rates of 3 and $10mm/s$. As a thought experiment, envision that the initial flow rate was

$10mm/s$ and then decreased to $3mm/s$ due to an intervention (i.e., laser, stimuli, drug. etc). Figure 3.5 shows the flow rate maps predicted with the mLSI model $[equation 3.1]$.

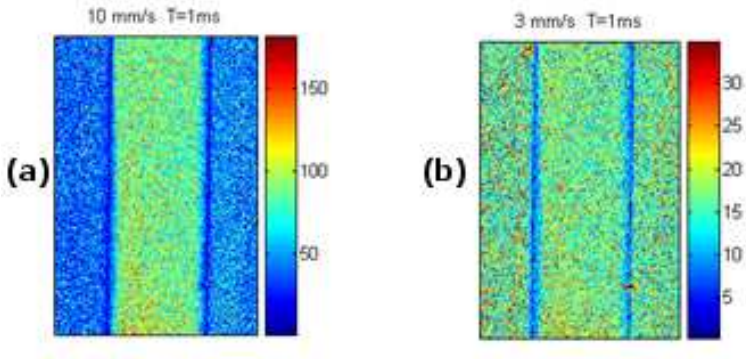

Figure 3.5: Maps of in vitro flow rates predicted with the mLSI model for actual flow rates of (a) 10mm/s and (b) 3mm/s.

Figure 3.6 shows the SFI maps predicted with our model Eq. 3.6] for the same flow rates $10mm/s$ and $3mm/s$. Since equation 3.5 allows for consideration of image exposure time, both images were acquired in the linear response ranges of their corresponding exposure times, $T = 1$ and $10ms$ respectively (see figure 3.3).

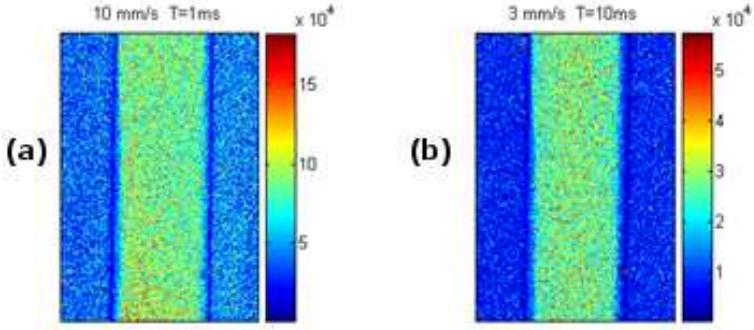

Figure 3.6: Maps of in vitro flow rate predicted with our modified mLSI model (equation 3.5) for actual flow rates of (a) $10mm/s$ and (b) $3mm/s$. Exposure times of 1 and $10ms$ were used to work within the linear response range of our instrument for the two actual flow rates.

To calculate the relative flow rate changes predicted by $1/N_t$ and SFI from figures 3.5 and 3.6, respectively, we selected a $300x100$ subregion of pixels within the tube and then calculated the corresponding mean values (Table 3.1). The actual relative flow rate change was 3.33. The conventional mLSI model [equation 3.1] predicted a relative flow rate change of 5.2, and our model [equation 3.5] predicted a relative flow rate change of 3.16, or a relative error of 56.15% and 5.1% respectively.
In Table 3.2, we calculated the relative flow rate change for an additional thought experiment in which the initial flow rate of $9mm/s$ is assumed to decrease to $2mm/s$.

Table 3.1: Relative flow rate change and $\%$ relative error predicted by the equations (1) and (6) from figures 4 and 5 respectively.

T (ms)	Flow rate (mm/s)	$1/N_t$ (a.u.)	SFI (s-1)
1	10	91.58	91581
1	10	17.59	N/A^{**}
10	3	N/A^{*}	28943
RFVC	10/3=3.33	91.58/17.59=5.2	91581/28943=3.16
relative error	N/A	56.15	5.1

N/A^{*}: Not Applicable because the parameter 1/Nt does not take into account the exposure time.
N/A^{**}: Not Applicable because the SFI associated with this exposure time is out of the linear response range.

Table 3.2: Relative flow rate change and $\%$ relative error predicted with equations (1) and (5).

T (ms)	Flow rate (mm/s)	$1/N_t$ (a.u.)	SFI (s-1)
1	9	83.491	83491
1	2	4.907	N/A^{**}
10	2	N/A^{*}	24744
RFVC	9/2=4.5	83.491/4.907 =17.01	83491/24744=3.37
relative error	N/A	278	25.1

N/A^{*}: Not Applicable because the parameter 1/Nt does not take into account the exposure time.
N/A^{**}: Not Applicable because the SFI associated with this exposure time is out of the linear response range.

For this second example, the actual relative flow rate change was 4.5. The conventional mLSI model predicted a relative flow rate change of 17.01, and our model a change of 3.37, or a relative error of 278% and 25.1% respectively.
An unexpected finding was the large difference in relative errors observed in the two separate experiments summarized in Tables 3.1 and 3.2 (5% and 25%, respectively). We propose that the fivefold difference in relative error, may be due in part to the complex motion we anticipate may exist during our experiments, especially at low flow rates. At these flow rates, the relative degree of Brownian motion and ordered motion is unknown, and therefore a more realistic model may be required [41]. Further study is warranted. Nevertheless, despite the difference in relative errors, data from both experiments strongly support our central hypothesis that exposure time must be integrated into the conventional mLSI algorithm to improve its accuracy by as much as one order of magnitude.

3.4 Conclusions

- Based on Goodmans theory of time-integrated intensity of thermal or pseudothermal light, we have incorporated the image exposure time into the mLSI equation, resulting in equation 3.6.
- We have validated our approach with experimental data collected from a flow

phantom. Use of equation 3.6 over the conventional mLSI equation 3.2 enables a substantial improvement in the accuracy of assessing flow rate changes using mLSI.

- The theory and the results shown in this chapter were published in: J. C. Ramrez-San-Juan, Y. C. Huang, N. Salazar-Hermenegildo, R. Ramos-Garca, J. Muoz-Lopez and B. Choi. Integration of image exposure time into a modified laser speckle imaging method, Phys. Med. Biol. 55, 6857-6866, (2010).

Chapter 4

Effects of speckle/pixel size ratio on temporal and spatial speckle-contrast analysis of dynamic scattering systems: Implications for measurements of blood-flow dynamics

Because the dynamic range of laser speckle contrast imaging is closely related to the range of measurable speckle contrast values. This range itself is linked to several experimental parameters, including source coherence length, analysis algorithm approach (i.e., temporal vs. spatial analysis), and the spatial sampling of the speckle pattern [41, 44]. This chapter deals with the discussion related to the proper spatial sampling of speckle pattern.
The ratio speckle $area/pixel$ area defines the parameter N employed in the following plots.
The key governing equation involves the minimum-resolvable speckle size [44, 45]. In chapter two we defined the minimum size of speckle as β,

$$\beta = 1.22(1 + M)(f/\#)\lambda \tag{4.1}$$

where M is the optical magnification, $f/\#$ the f-stop of the imaging optics, and λ the optical wavelength of the coherent source. Historically, experimental parameters were chosen to match approximately β with the pixel pitch of the imaging sensor. However, in order to satisfy the Nyquist sampling criterion and maximize the contrast of the imaged speckle pattern, Kirkpatrick et al. [41] used an in-vitro experimental setup to demonstrate that pixel size should be at least twice the pixel size. This finding was supported by computer simulation data from Thompson et al. [44]. The data from Kirkpatrick represent one extreme condition, in which the speckle pattern consists solely of static speckle. However, in biological samples, a mixture of static and dynamic con-

tributions to the imaged speckle pattern is expected. As a consequence, blurring of the image and subsequent decrease of the maximum achievable speckle contrast due to spatial and temporal integration of the light is produced.

4.0.1 Flow phantom

The flow phantom consists of a micro-channel slide (thinXXS Microtechnology AG) with channels of $300 - \mu m$ diameter. The slide was placed on a rigid resin substrate polymerized with a suspension of $TiO2$ particles to simulate the scattering properties of human skin, figure 4.1. A syringe-based infusion pump was used to induce flow of 1% Intralipid through the channels, at flow speeds from 4 to $20mm/s$ in step of $2mm/sec$.

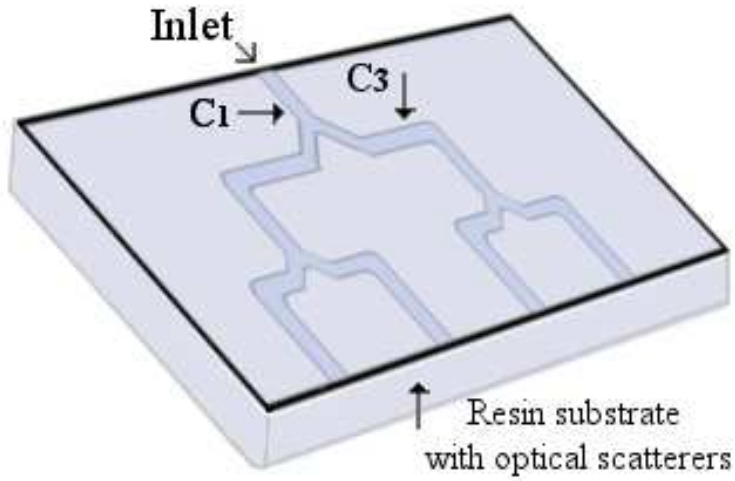

Figure 4.1: Skin phantom employed in this study. Intralipid was injected into the inlet, and K (contrast) and SFI (Speckle Flow Index) measurements were determined at regions within channels C1 and C3

4.0.2 Laser speckle contrast imaging (LSCI)

An expanded and collimated $532 - nm$ laser (Verdi, Coherent Inc.) illuminates an engineered diffuser, which in turn, homogenously illuminates the flow phantom, figure 4.2. Raw speckle images were acquired with a Retiga CCD camera ($7.4\mu m$ x $7.4\mu m$ pixel area) equipped with a macro lens with variable aperture. A linear polarizer was placed in front of the camera lens and its orientation is set to be perpendicular to that of the incident light's polarization to minimize specular reflection from the skin phantom. In order to modulate the speckle's size, and therefore the $speckle/pixel$ size ratio, we changed the $f/\#$ setting of the lens according equation 4.1, and the laser power was adjusted to achieve a consistent mean gray level measured from the CCD sensor.

The exposure time was fixed at 10 ms because this value is common for in-vivo LSI applications.

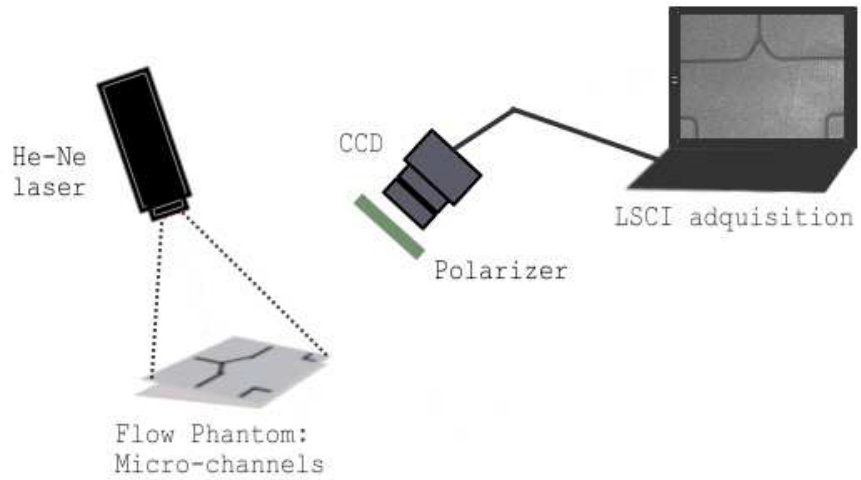

Figure 4.2: Experimental setup.

4.1 Experimental design and data analysis

For each flow speed setting, we collected a sequence of 30 raw speckle images. The sequences were processed using either temporal [32] or spatial [9] algorithms to calculate resultant speckle-contrast images. With the temporal algorithm, analysis was done on a pixelby- pixel basis, using the previously-published temporal LSI algorithm [32]. With the spatial algorithm, each of the 30 images was converted to corresponding speckle-contrast images, using a 5x5 sliding-window operator, and an average speckle contrast image was calculated. With the resultant speckle-contrast images, we focused our analysis on 30x100 regions of interest within channels C1 and C3.

4.2 Results and Discussion

Parthasarathy et al. [30] and [46] derived an equation that relates speckle contrast (K) and the correlation time (τ_c) of the backscattered light from the sample:

$$K(T,\tau_c) = \left[\beta\rho^2\frac{e^{-2x}+1-2x}{2x^2} + 4\beta\rho(1-\rho)\frac{e^{-x}-1+x}{x^2} + \beta(1-\rho)^2\right]^{1/2} \quad (4.2)$$

where $x = T/\tau_c$, T is the camera exposure time,$\rho = (I_f + I_c)/I_f$ is the fraction of total light that is scattered by moving optical scatterers, C_{noise} is a constant term that accounts for noise [30], and β accounts for the effect of spatial integration of the speckle pattern due to the finite size of the pixel [47, 48].

In the absence of static optical scatterers ($\rho = 1$) and noise ($C_{noise} = 0$), Eq. 4.2 simplifies to:

$$K(T, \tau_c) = \beta \frac{e^{-2x} + 1 - 2x}{2x^2}]^{1/2} \tag{4.3}$$

In the long exposure regime (i.e., $T >> \tau_c$) [37] and considering that the flow speed $V \propto 1/\tau_c \equiv SFI$ [49], Eq. 4.3 can be approximated by:

$$K = aV^{-1/2} \tag{4.4}$$

where a is a proportionality constant.
Figure 4.3 shows the average speckle contrast of a region within channel C1 obtained with the temporal (figure 4.3 a) and the spatial (figure 4.3 b) contrast analysis as a function of the actual flow speed, for different values of N (number of pixels per speckle, i.e. the area of the speckle divided y the area of the pixel). From our experimental results (figures 4.3 a) and 4.3 b), for predominantly dynamic speckle, the speckle contrast depends on the spatial sampling of the speckle pattern, with both temporal and spatial speckle-contrast analysis. Eq. 4.4 fits the temporal- and spatial-contrast data well for all experimental values of N (figure 4.3), although the fit is less accurate for the latter.

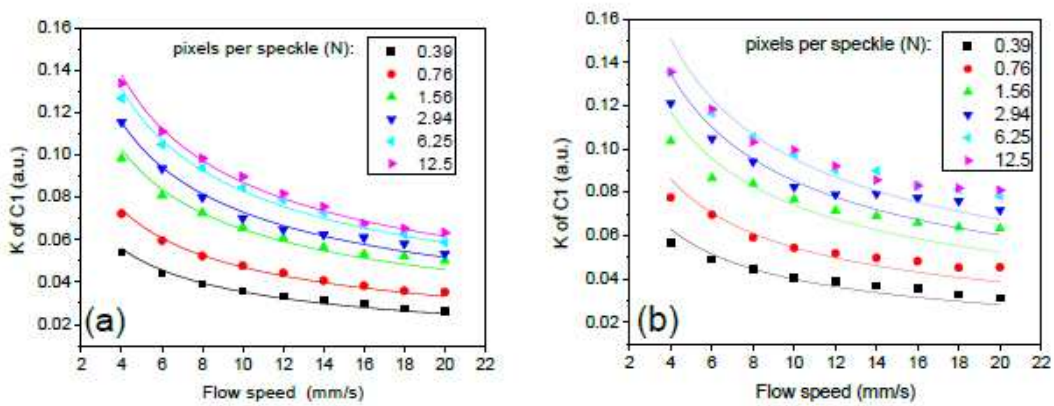

Figure 4.3: Average speckle contrast of a region within channel C1, vs. flow speed, for different ratios of spatial sampling of the speckle pattern (e.g., pixels-per-speckle values) for (a) temporal and (b) spatial speckle contrast analysis. The symbols represent experimental data and the solid lines are the corresponding fits to Eq. 4.4.

For dynamic scattering, K increases with an increase in N (Figure 4.4). A notable difference between the data in figure 4.4 and those from [41] is that K increases even for N values greater than two, i.e. there is still a reduction on the speckle contrast due to the spatial averaging of the speckle pattern in turn due to the finite pixel-size. With a static scattering substrate, the data from [41] reached a plateau value for all $N > 2$.
Since most experimental studies involve use of LSI to assess relative changes in blood flow, an important practical question is to assess how relative flow speed measurements

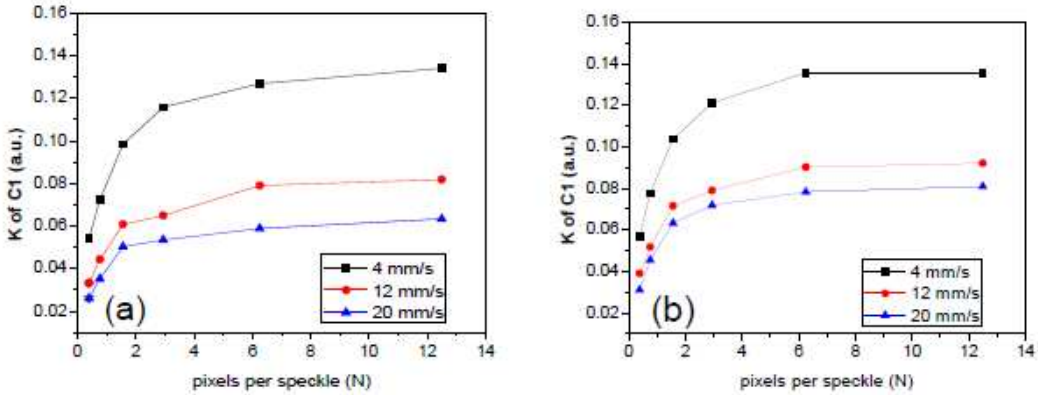

Figure 4.4: Relative flow speed [e.g., (SFI in C1)/(SFI in C3)] is only weakly dependent on N and actual flow speed. The dependence is noticeably weaker with the (a) temporal speckle contrast approach than with the (b) spatial speckle contrast approach.

(i.e., relative changes in SFI) are affected by N. Our experimental data demonstrate that, over a large range of N values (0.39 to 12.5) and flow speeds (up to 20 mm/s), the relative change in SFI is the same (figure 4.5). For example, the ratio in SFI values between channels C1 and C3, is equal to 2 for each of the N values used in this study; this ratio is in agreement with the expected ratio in flow speed based on the relative dimensions of the two channels. Note that the ratio is more accurate with temporal contrast analysis (figure 4.5 a) than with spatial contrast analysis (figure 4.5 b); while the relative flow speed remains at a value of 2 with temporal analysis, it decreases linearly with actual flow speed when spatial analysis is used. A similar decrease was observed using various sliding-window sizes (5x5, 7x7 and 9x9) [50].

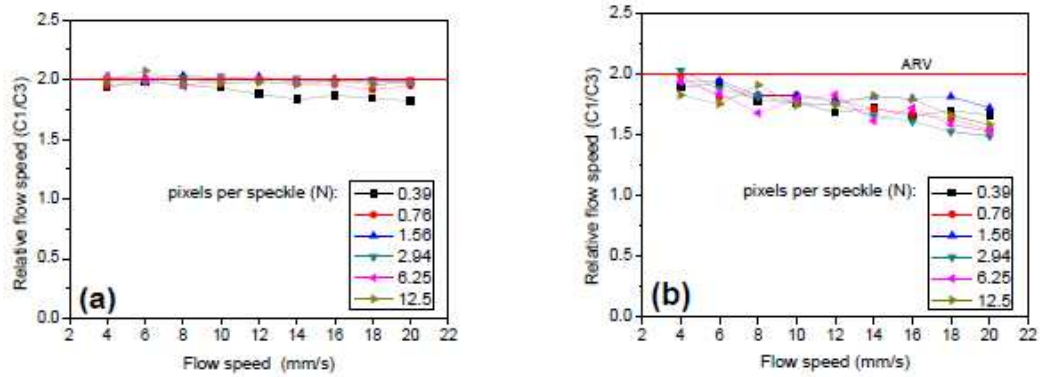

Figure 4.5: Relative flow speed [e.g., (SFI in C1)/(SFI in C3)] is only weakly dependent on N and actual flow speed. The dependence is noticeably weaker with the (a) temporal speckle contrast approach than with the (b) spatial speckle contrast approach.

This difference between the spatial and temporal analysis on the relative flow speed is an unexpected finding, previously, it was thought that the difference between the two algorithms was only in the spatial and temporal resolution of the speckle contrast images obtained from them. Recently Parthasarathy et al. [30] suggested that the spatial algorithm is more sensitive to the static component of the scattered light compared with the temporal algorithm. Based in this hypothesis, we explain the linear decay in Fig. 4.5 b as follow. Let suppose (see Eq. 4.2) Ks,C1 is the spatial contrast on channel 1 (C1 in Fig 4.1)

$$K_{s,C1}^2 = \beta\rho^2 \frac{e^{-2x} + 1 - 2x}{2x^2} + 4\beta\rho(1-\rho)\frac{e^{-x} - 1 + x}{x^2} + \beta(1-\rho)^2 \tag{4.5}$$

Therefore, given that the velocity in C3 is half the velocity in C1, the spatial contrast on C3 is given by:

$$K_{s,C3}^2 = \beta\rho^2 \frac{e^{-2x/2} + 1 - 2x/2}{2x/2^2} + 4\beta\rho(1-\rho)\frac{e^{-x/2} - 1 + x/2}{x/2^2} + \beta(1-\rho)^2 \tag{4.6}$$

From Refs [30, 46] the last two terms in Eq. 4.5 appears only when the static component of the light is taken into account and given that the temporal algorithm is not sensitive to the static component of the light, then the temporal contrast for C1 and C3 are given by:

$$K_{s,C1}^2 = \beta\rho^2 \frac{e^{-2x} + 1 - 2x}{2x^2} + 4\beta\rho(1-\rho)\frac{e^{-x} - 1 + x}{x^2} + \beta(1-\rho)^2 \tag{4.7}$$

$$K_{s,C1}^2 = \beta\rho^2 \frac{e^{-2x/2} + 1 - 2x/2}{2x/2^2} + 4\beta\rho(1-\rho)\frac{e^{-x/2} - 1 + x/2}{x/2^2} + \beta(1-\rho)^2 \tag{4.8}$$

In the long exposure regimen (i.e., $T \gg \tau_c$) the relative flow speed (RFS) is given by:

$$RFS = \frac{SFI_{C1}}{SFI_{C3}} = \frac{K_{C3}^2}{K_{C1}^2} \tag{4.9}$$

Where the Speckle Flow Index (SFI) on C1 is given by $SFI_{C1} = 1/(TK_{C1}^2)$. Figure 4.6 shows the RFS as a function of x (which is proportional to the flow speed) for the temporal algorithm (solid line) and the spatial (segmented lines) algorithm for different values of ρ.

In Fig. 4.6, the RFS for the temporal algorithm is independent on ρ, it means that the tree curves (for the three values of ρ) are overlapped on the continuous one. Even when there is a small amount of static light (1 or 2 %), the RFS decreases linearly for the spatial analysis, these results explain the differences between the temporal and spatial analysis shown in Fig. 4.5.

Meanwhile we can state that, while absolute measurements of speckle contrast are strongly affected by a change in N (figures 4.3 and 4.4), the relative flow speed is minimally affected by N (figure 4.6).

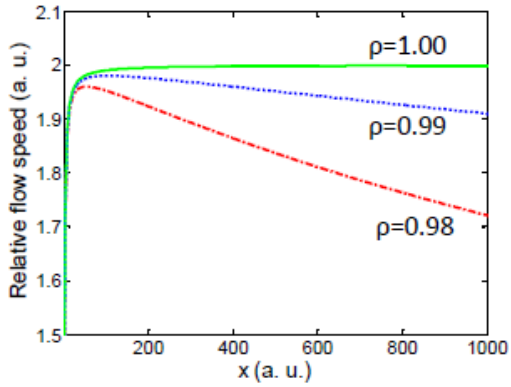

Figure 4.6: RFS as function of x for different values of ρ, while the RFS for the temporal algorithm keeps constant around 2 for different values of ρ (continuous line), the RFV for the spatial algorithms is very sensitive to any change of this parameter, i.e. it is very sensitive to the static light even as small as 1% of the total light.

4.3 Conclusions

- Our in-vitro experimental data collected from a dynamic-scattering phantom demonstrate that speckle contrast increases with an increase of N, even at values beyond the Nyquist sampling criterion of N = 2. For monitoring of relative changes in blood flow, however, the relative change in SFI is minimally affected by N and flow speed, over a large range of values for the two parameters. Use of the temporal LSCI algorithm, is more accurate at assessing relative changes in blood flow, especially at faster flow speeds, than the spatial LSCI algorithm. Based on these findings, we recommend that, for measurement of relative changes in blood flow in samples with minimal motion artifact, such as a rodent brain fixed in a stereotactic frame, that the temporal LSCI algorithm be used

- The theory and the results shown in this chapter were published in: J. C. Ramirez-San-Juan, E. Mendez- Aguilar, N. Salazar-Hermenegildo, A. Fuentes-Garcia, R. Ramos-Garcia, and B. Choi. *Effects of speckle/pixel size ratio on temporal and spatial speckle-contrast analysis of dynamic scattering systems: Implications for measurements of blood-flow dynamics* , Biomed. Opt. Express 4(10),1883-1889, (2013).

Chapter 5

Trans-illumination Breast Spectroscopy System TiBS for the assessment of breast health

5.1 Introduction

Breast cancer is a worldwide health problem. Many research has been carried out in order to understand the causes of this disease. By using light with different energy has been possible to see inside human body in a non-invasive way. Breast cancer is a disease which has been widely studied with either ionising or non-ionising radiation, for instance Trans-illumination spectroscopy which is a non-ionising technique [51]. This chapter develops roughly the work done about the project: Trans-illumination Breast Spectroscopy System (TiBS) for the assessment of breast health. Introduces the impact of breast cancer on women, establish the motivation for this work, present the currents methods for breast imaging and introduces the potential modality to get physiological properties of breast tissue by using trans-illumination spectroscopy, finally presents some partial results. Lets begin presenting some relevant statistics about of breast cancer in women.

5.2 Breast cancer statistics

According to the World Health Organization WHO, breast cancer is, by far, the most frequent cancer among women with an estimated 1.67 million new cancer cases diagnosed in 2012 (25% of all cancers), figure 5.1.
In Mexico, breast cancer occupies today first in incidence of malignant neoplasms in women as is shown in figure 5.2 [52].
In 2011, the highest incidence of mammary neoplasia among women aged 20 and older, is located in the population of 60-64 years of age (61 new cases per 100,000 women), followed by women 50-59 years (51 cases per 100 000) and those of 45-49 years (45

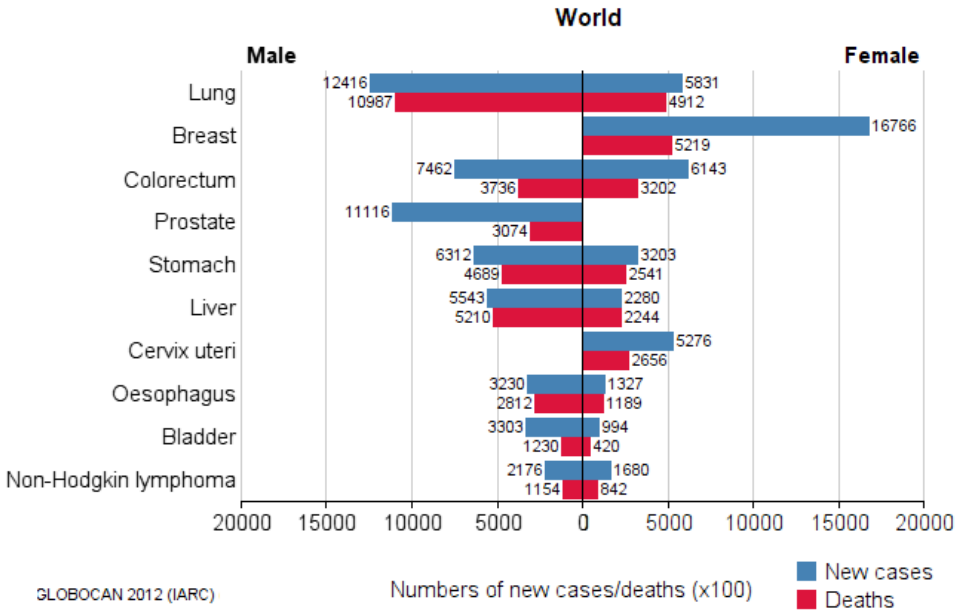

Figure 5.1: Breast Cancer. Incidence/Mortality Worldwide in 2012

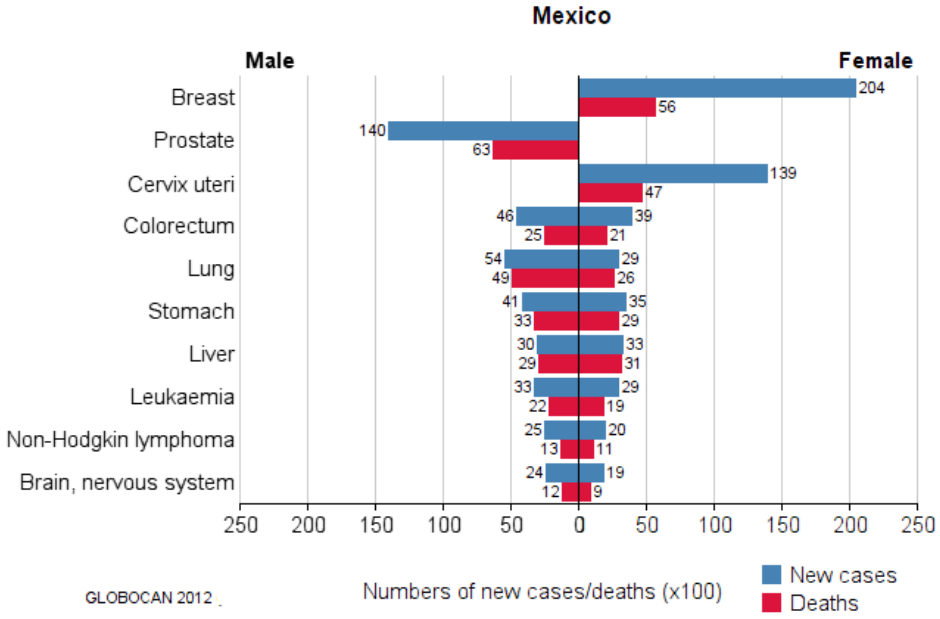

Figure 5.2: Breast Cancer. Mexico Incidence/Mortality in 2012

new cases). Figure 5.2 shows that breast cancer is less common in young women than at older age [53].

Another measure that allows us to observe the impact of breast cancer among women, is the hospital case fatality rate, with which the number of dead people is obtained by

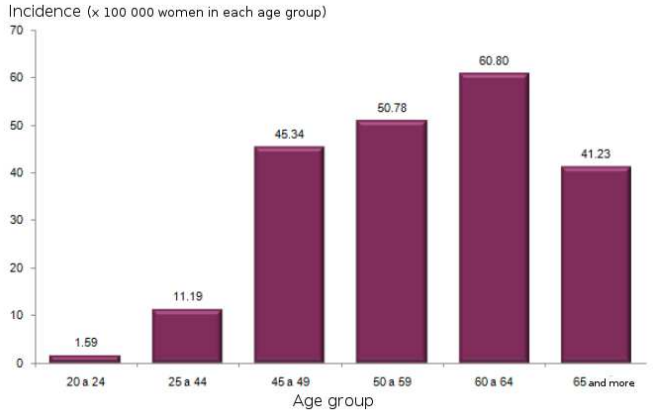

Figure 5.3: Incidence of malignant breast tumor in women aged 20 years and over by age group, 2011.

this disease to total hospital discharges 5.2.

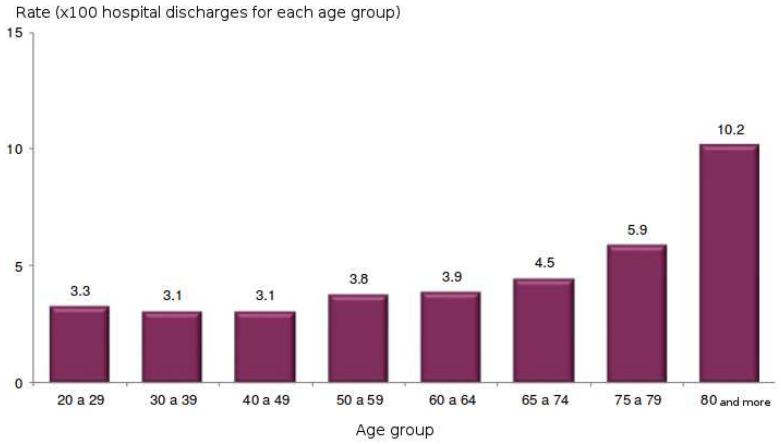

Figure 5.4: Breast Cancer hospital case fatality rate, in women of 20 years and more by age group, 2012.

For 2012, it is observed that after 40 years, this rate increases as the age of the woman increases and peaks in those aged 80 and over, at death 10 out of 100 women with cancer. This can be explained considering that the older is more likely with the cancer are present other chronic degenerative diseases that hinder the body's response to treatment options (surgery, chemotherapy or radiotherapy) and due to the aggressiveness of the tumor itself [53]. Although breast cancer in younger women (20-29) is less common than older age (50 and more), the fatality in younger women is still high in comparison with older women, see figure 5.2. This shows that the age is a high risk factor of death because breast cancer. Next section stablish the motivation for this work.

5.3 Motivation

Gender, Age, Race, Family history, Menstrual and Reproductive History, Certain Genome Changes (genes, such as BRCA1 and BRCA2), are genetic risk factor that are associated with breast cancer all of these are not within our control, however others, especially those related to personal behaviours, can be modified. It is important to know about risk factors because they can help identify women who might benefit from certain preventive strategies including changing behaviours. It is therefore of importance begin an assessment of breast health at earlier age. In this regard non-invasive optical techniques have been created to assess breast health. In this thesis we focus in trans-illumination breast spectroscopy.

5.4 Breast anatomy

The breast is a mass of glandular, fatty, and fibrous tissues positioned over the pectoral muscles of the chest wall and attached to the chest wall by fibrous strands called Cooper′s ligaments figure 5.4. A layer of fatty tissue surrounds the breast glands and extends throughout the breast. The glandular tissues of the breast house the lobules (milk producing glands at the ends of the lobes) and the ducts (milk passages). During lactation, the bulbs on the ends of the lobules produce milk. Once milk is produced, it is transferred through the ducts to the nipple [54].

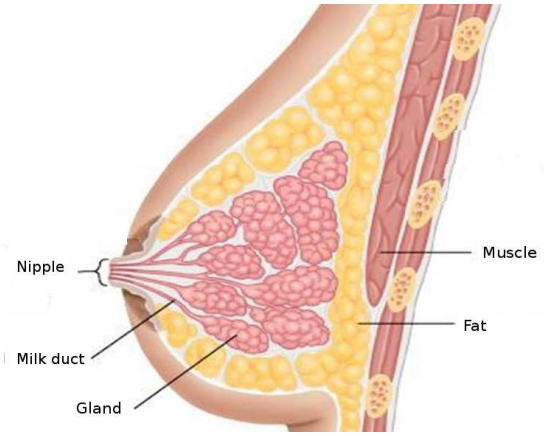

Figure 5.5: Lateral view of the female breast, Adapted from [54].

5.5 Breast cancer

Breast cancer refers to a malignant tumor that has developed from cells in the breast. Normally, the cells in our bodies replace themselves through an orderly process of cell growth: healthy new cells take over as old ones die out. But over time, mutations can

turn on certain genes and turn off others in a cell. That changed cell gains the ability to keep dividing without control or order, producing more cells just like it and forming a tumor. A tumor can be benign, i.e not dangerous to health and are not considered cancerous, or malignant which means that has the potential to be dangerous and are cancerous.
Usually breast cancer either begins in the cells of the lobules, which are the milk-producing glands, or the ducts, the passages that drain milk from the lobules to the nipple. This determines the type of cancer and are considered as:

- Non-invasive breast cancer: Ductal Carcinoma In Situ (DCIS): abnormal cells were formed within the milk ducts and are still contained there. It is an early-stage breast cancer and is considered as a precancerous condition. Indeed, if not treated it can progress to form an invasive breast cancer.

- Lobular Carcinoma In Situ (LCIS): abnormal cells were formed within the lobules of the breast and are still contained there. It is a precancerous condition but it is not clear whether LCIS is an early-stage breast cancer. LCIS is a risk factor of developing breast cancer and therefore can be left untreated with a yearly mammographic follow up.

- Invasive breast cancers: It is called Invasive Ductal Carcinoma (IDC) when cancer cells from the milk duct invade the surrounding breast tissue. It represents the majority of breast cancers. Another type of cancer is called

- Invasive Lobular Carcinoma (ILC) when it initially forms within the milk lobule and invades the surrounding breast tissue this type of cancer is less common than IDC and is often more difficult to diagnose on mammogram and by palpation (there is no breast lump). Invasive breast cancers can also metastasize through the blood stream or lymphatic vessels to other parts of the body.

A screening test tries to find a disease before there are any symptoms. The mammogram is the main imaging tests recommended to find breast cancer early. Next section deals with breast cancer imaging techniques.

5.6 Breast Imaging Tests

With mammogram lesion identification relies on the imaging of radiographic density differences between different tissue types. Breast density is a way to describe the composition of a woman′s breasts. This measure compares the area of breast and connective tissue seen on a mammogram to the area of fat. Breast and connective tissue are denser than fat and this difference shows up on a mammogram. High breast density means there is a greater amount of breast and connective tissue compared to fat. Low breast density means there is a greater amount of fat compared to breast and connective tissue. High breast density, as seen on a mammogram, is linked to an increased risk of breast

cancer. Women with very dense breasts are four to five times more likely to develop breast cancer than women with low breast density [56, 57]. However mammography has limitations, one of this are a false-positive mammogram which looks abnormal but no cancer is actually present it is more common in women who are younger, have dense breasts, have had breast biopsies.
There are other imaging techniques are emerging to overcome the limitations of mammography, and some of them are already used as adjunctive screening tools. Some of these are [58]:

- Digital mammography. The use of a computer, rather than x-ray film, to create a picture of the breast.
- Magnetic Resonance Imaging (MRI). A procedure in which radio waves and a powerful magnet linked to a computer are used to create detailed pictures of areas inside the body. These pictures can show the difference between normal and diseased tissue. Magnetic resonance imaging makes better images of organs and soft tissue than other scanning techniques, such as computed tomography (CT) or x-ray. To improve the ability of the MRI to clearly show abnormal breast tissue a contrast material (called gadolinium) is injected into a vein (IV) in the arm during the exam. Their limitations are MRI scans can take a long time, MRI is expensive and invasive.
- Positron Emission Tomography (PET) scanning. A procedure in which a small amount of radioactive glucose (sugar) is injected into a vein, and a scanner is used to make detailed, computerized pictures of areas inside the body where the glucose is taken up. Because cancer cells often take up more glucose than normal cells, the pictures can be used to find cancer cells in the body. Also called PET scan.

Because tumors have distinct compositions that differ from healthy breast tissue the techniques mentioned above are used as adjunctive screening tools. While mammography are based on morphological information of breast tissue, MRI and PET can give functional and molecular characteristics specific to tumors.
X-ray creates the mammogram image, radio waves creates a MRI image and Gamma ray creates a PET image, all of these different form of energy which are sensitive to different types of biological components. As these, there are techniques based on optical non-invasive radiation which can provide functional and molecular characteristics and are cost-effective. Next section deals with optical techniques which can reveal physiological information that is not available whit the conventional methods.

5.7 Optical breast tests

Diffuse Optical Tomography uses Near-infrared (NIR) light to form images of the interior of body. In the Near-infrared region the absorption of light by tissue is relatively

low. As a result, there is a window in the NIR from about 650-950 nm where light can penetrate more deeply into tissue. Trans-illumination spectroscopy employs the same optical window to get breast tissue physiological information. For this range of wavelength light transmitted through 10 cm of human breast tissue can be detected because transmitted photons will have been randomly scattered multiple times so that they propagates into the tissue diffusely. In order to discuss the technique of trans-illumination spectroscopy in more detail, it is important to know the optical properties of tissue and to establish an understanding of the manner in which light propagates through biological tissue. Next section therefore describes the mechanisms that govern light transport through physical media and identifies the components of biological tissue that are responsible for these processes.

5.7.1 Light propagation in biological tissue

Once the light reaches the skin, part of it is absorbed, part is reflected or scattered, and part is further transmitted figure 5.1.

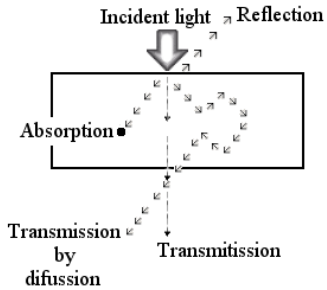

Figure 5.6: Light-tissue interaction.

The propagation of the photons can be modelled by a Diffusion Model for infinite slab geometry [59]. Light propagation in tissue is determined by scattering, described by the scattering coefficient μ_s , and absorption, described by the absorption coefficient μ_a, both of which are dependent on cellular structure and molecular composition of the tissue [59]. The reciproce of both coefficients describe the average pathlength the photons travel before being scattered or absorbed. Because of refractive index discontinuities between and within cells, most biological tissues have an inhomogeneous structure and are therefore highly scattering. Within the trans-illumination wavelength range, the probability of a scattering event is much larger than the probability of an absorption event. After a sufficient number of light scattering events, the propagation direction of the photon has become independent of the propagation direction of the incoming photon. Scattering in biological tissues is then characterized in terms of reduced scattering coefficient $\mu_s^{'}$,which is defined as the product of the scattering coefficient and one minus the anisotropy factor $(1 - g)$. The anisotropy factor g is defined as the average of the cosinus of the scattering angle. The optical methods examining biological tissues

for this regime are then referred to as diffuse optical methods [59]. With an accurate model of how the light propagates, experimenters can then use the light they detect, to gain information about the tissue through which it has passed, including the concentration of absorbing chromophores such as oxy and deoxy-hemoglobin, water, collagen and lipids and the amount of light scattering.

5.7.2 Chromophore concentration

The overall effect of absorption is a reduction in the intensity of the light beam traversing the medium. Mathematically the absorption of light in a purely absorbing medium and the thickness of the medium is given by the relationship known as the Lambert-Bouguer law

$$\frac{dI}{I} = \mu_a dl \tag{5.1}$$

which describes how each successive layer dl of the medium absorbs the same fraction dI/I of the incident intensity I for a constant μ_a, the latter known as the absorption coefficient with units of inverse length (usually mm^{-1}). For an incident intensity I_0, therefore, the transmitted intensity I through a distance l will be

$$I = I_0 e^{-\mu_a l} \tag{5.2}$$

The absorption coefficient μ_a can thus be interpreted as the probability that a photon will be absorbed by the medium per unit length. The reciprocal of the absorption coefficient, known as the absorption length, is the distance required for the intensity of the beam to fall to e^{-1} of the initial intensity. When Equation 5.2 is expressed in base 10 logarithms

$$I = I_0 10^{Kl} \tag{5.3}$$

then the constant K is known as the extinction coefficient. The absorbance of the medium is defined as the $log_1 0$ ratio of the incident and transmitted intensities

$$A = log_{10}\left(\frac{I_0}{I}\right) = Kl \tag{5.4}$$

where the unit of absorbance is the *optical density* (OD). Hence, the units of K are OD per unit length (usually OD cm^{-1}). The extinction coefficient and the absorption coefficient are conceptually the same, differing only by the base of the logarithm used in the Lambert-Bouguer expression. For the same unit length, therefore, the extinction coefficient is related quantitatively to the absorption coefficient by a factor of 0.434.
The absorption coefficient of a compound is linearly related to its concentration c diluted in a non-absorbing medium

$$\mu_a = \alpha c \tag{5.5}$$

where α is known as the specific absorption coefficient. Substituting for μ_a in the Lambert- Bouguer law gives what is known as the Beer-Lambert law

$$I = I_0 e^{\alpha c l} \tag{5.6}$$

Expressing the Beer-Lambert law in log_{10} gives

$$I = I_0 10^{\epsilon c l} \tag{5.7}$$

where ϵ is the specific extinction coefficient, usually expressed in units of OD cm^{-1} mM^{-1}. In a solution containing a mixture of n absorbing compounds, the total absorbance is the sum of the individual extinction coefficients multiplied by the distance l

$$\begin{aligned} A &= (K_1 + K_2 + \ + K_n)l \\ &= (\epsilon_1 c_1 + \epsilon_2 c_2 + \ + \epsilon_n c_n)l \end{aligned} \tag{5.8}$$

There are many compounds in biological tissue which absorb light radiation, collectively known as tissue chromophores, each of which has its own unique spectrum. As expressed in Equation 5.8, the total extinction coefficient of a mixture of compounds is equal to the sum of their individual extinction coefficients, weighted by their relative concentrations. Therefore, approximating tissue as a homogeneous mixture of compounds, the overall light absorption in tissue at a given wavelength depends on the type and concentration of chromophores present. Figure 5.7 shows the chromophores present in biological tissues and their absorption spectra.

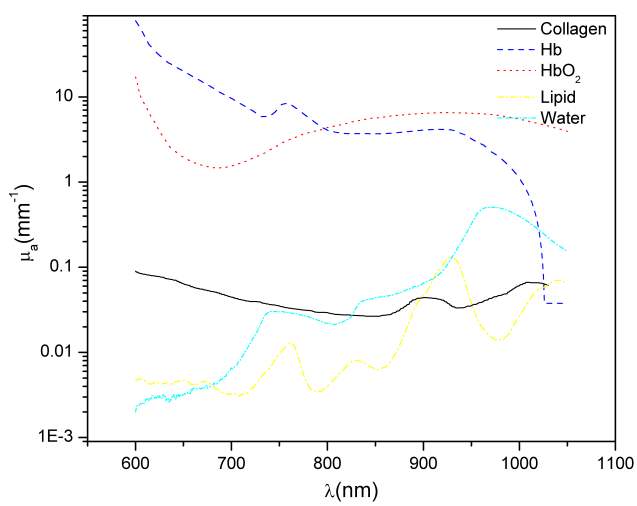

Figure 5.7: Chromophores present in biological tissues and their absorption spectra.

5.8 Methods

In this work an Nelder-Mead [60] simplex algorithm was used to calculate the minimum error between the guess chromophore value and the experimental. The algorithm works according to following flowchart, figure 5.8,

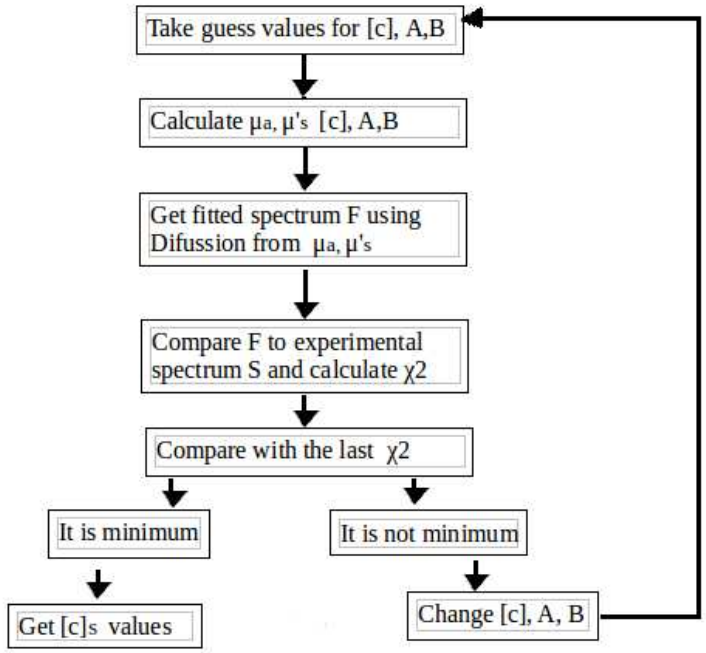

Figure 5.8: Flowchart algorithm to calculate the chromophore concentration $[c]_S$.

Guess values for chromophore concentration were used as a matrix $[c]$ and A,B are the reduced scattering coefficients $\mu_s^{'} = A\lambda^{-B}$. The chromophore concentration were obtained by chi-square (χ^2) minimization of the difference between the measured $S(\lambda)$ and Fit $F(\lambda)$ spectrum by:

$$\chi^2 = \Sigma\sqrt{\frac{(S(\lambda) - F(\lambda))^2}{S(\lambda)^2}} \tag{5.9}$$

5.9 F(λ) calculation

$F(\lambda)$ is a theoretical spectrum which is calculated from the guess values for chromphore concentration and the A, B scattering parameters by using the Diffusion equation. Diffusion equation is solved for a scattering media with refractive index mismatched boundary conditions. This conditions refers to the difference on the refraction index between the ambient and scattering media, in this case air and tissue [59]. Figure shows the calculated $F(\lambda)$ and experimental $S(\lambda)$ spectrum.
There are some restrictions that must be taken into account to aviod unrealistic chromophore values. All concentrations should be positive or zero and the sum of all of these should not exceed the unity. If not a penalty must be applied. The amplitude of fit

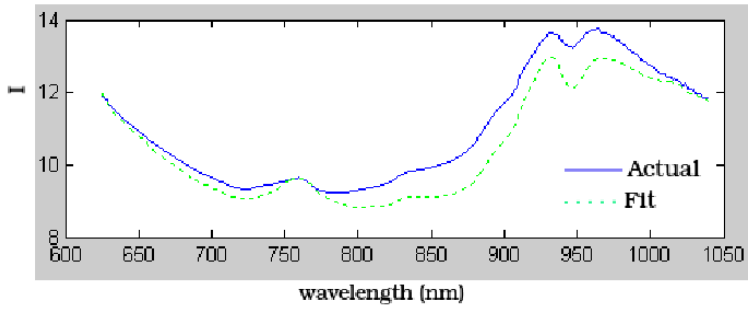

Figure 5.9: Fit$F(\lambda)$, and actual $S(\lambda)$ spectrum.

spectrum should be the same as the actual spectrum. If not a penalty must be applied.

5.10 TiBS set up and Data Collection

The TiBS set up consist of 50W halogen lamp as source whit a broadband from 550 to 1100 nm. The light emitted by the source is delivered to the breast tissue by a 5 mm diameter fibre bundle (Fibre Guide, Bridgeport, CT). Transmitted light is collected by a 3 mm diameter optical fibre bundle (Optica, Kitchener, Canada). A spectro-photometer (Kaiser, California, USA) with holographic trans-illumination grating (15.7rules/ mm blazed at 850nm) creates the trans-illumination spectra which is recorded bya a CCD (Photometrics, New Jersey, USA). The spectrometer is cooled by a cryogenically.
2193 spectra from the Density Study group (Mammography density). The participants were recruited From the Princes Margaret Hospital, Toronto, Canada between 2001 and 2004. Measurements of transmitted light. These were executed in four positions: center, medial, distal, lateral on left and right breast. Measurements are taken in a dark background to avoid luminosity noise.

5.11 Data correction

In a compound spectral system with multiple optical elements as TiBS, the measured spectra are not simply the spectra of the sample being measured, but rather a convolution with the emission spectra of the lamp, the efficiency profile of the grating, the transmission profiles of the optics and the quantum efficiency of the CCD camera. It is not the sample that is measured, but a superposition of the spectral characteristics of all elements in the system.
In order to compensate and remove these undesired elements from the signal a standardized attenuator is needed. As the sample will attenuate the intensity by 5 to 7 orders of magnitude a detector with a linear response of 7 to 9 orders of magnitude, including the AD converter is needed to attenuate the source intensity I_0 in a controlled

fashion. A ultra-high density polyurethane White Block WB is employed to have the trans-illuminated light exiting as a Lambertian emitter as the biological tissue. The corrected participant spectrum $S_{corr}$is expressed mathematically as

$$S_{corr}(\lambda) = log_{10}\frac{S_{part}(\lambda)}{S_{WB}(\lambda)} \tag{5.10}$$

where $S_{part}(\lambda)$ is the raw spectrum from participant and $S_{WB}(\lambda)$ is the white block corrected. However the white block correction can not be calculated directly because the sample reduces the source power by a 10^{-5} to 10^{-7}. Hence the detector can not obtain I_0. An attempt was made to attenuate the source by using a 1.4 mm pinhole, so the white block correction is given by

$$S_{WB}(\lambda) = log_{10}\frac{S_{wb}(\lambda)}{S_{pinhole}(\lambda)} \tag{5.11}$$

where $S_{wb}(\lambda)$ is the raw withe block spectrum and $S_{pinhole}(\lambda)$ is the spectrum from a pinhole used as attenuated source. Practical and optical problems impeded its use. Figure $refpinholes$ show that white block correction spectrum is not reproducible by using the pinhole as raw source spectrum because this varies with the position in which the pinhole is.
Lack of a standard reference attenuator will affect the subsequent analysis on estimation of chromophore concentration. To address this issue the white source was replaced by 13 laser in the same wavelength range and the transmitted spectrum was extrapolated in order to have a wavelength-independent detection system. The WB spectrum is shown in figure 5.11 As we can see the measurements from the two different systems agree very well so it is possible to employ this spectra for the correction data.

5.12 Partial Results

Once the spectra were corrected and converted to the OD units, the Matlab algorimth was employed to get the chromophore values over the hole Density Study spectra. Average value of chromophore concentration from the whole spectra are showed in fugure 5.12.
where

- 1=collagen
- 2=Hb
- 3=HbO_2
- 4=water
- 5=lipids

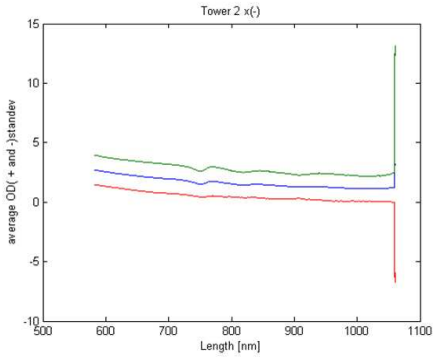

(a)

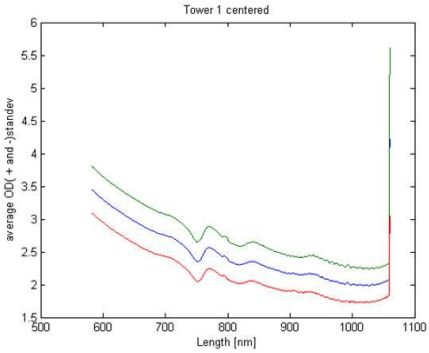

(b)

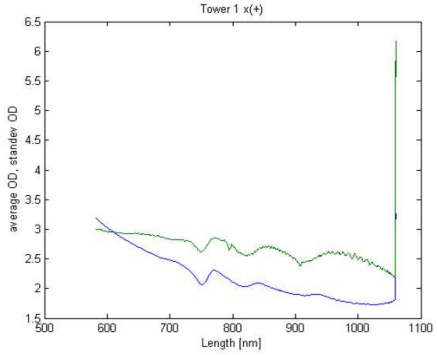

(c)

Figure 5.10: We show that white block correction spectrum is not reproducible by using the pinhole as raw source spectrum because this varies with the position in which the pinhole is

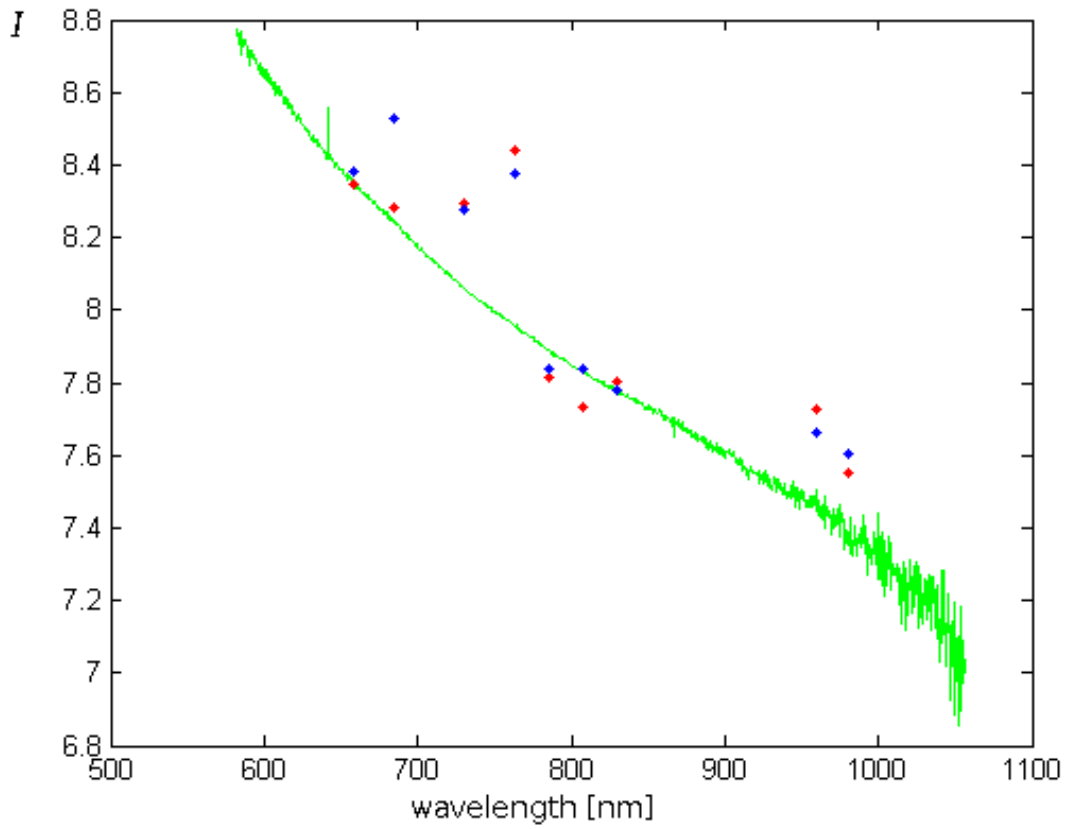

Figure 5.11: The white block spectrum measured with the TiBS system (continous line) and the spectrum measured with the lasers (points). Data provided by Jane Walter.

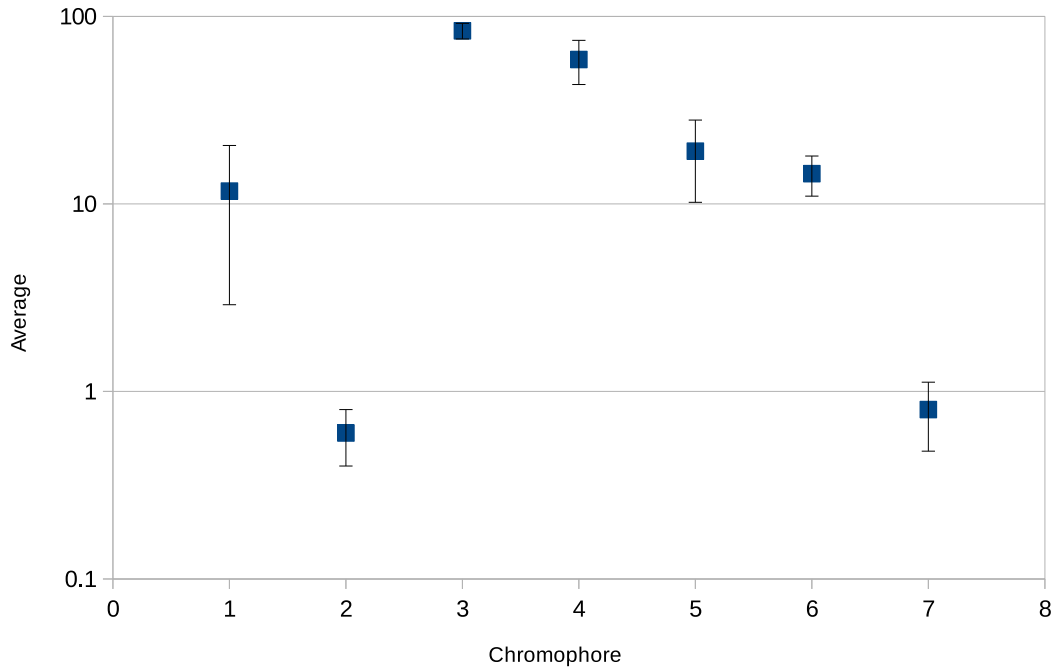

Figure 5.12: Chromophere average and standard deviation.

- 6=A
- 7=B

and A is the scattering coeficient value.

5.13 Conclusion

Trans-illumination spectroscopy is able to get chromophore values from real spectra. They may be useful for assessing physiologic tissue differences related to breast cancer risk. Due Trans-illumination spectroscopy is non-invasive it can be employed in younger women where mammography is not an option. As a future work a comparison of these values with other from literature is needed in order to establishes a confidence intervals.

Appendix A

Mammography physics

Radiography was the first medical imaging technology, made possible when the physicist Wilhelm Roentgen discovered x-rays on November 8, 1895. Mammography is radiography of the breast, and is thus a transmission projection type of imaging. Contrast in an image is the difference in the gray scale of the image. X-ray contrast is produced by differences in tissue composition, which affect the local X-ray absorption coefficient, which in turn is dependent on the density (g/cm^3) and the effective atomic number. The energy of the X-ray beam also affects contrast in X-ray images. Because bone has a markedly different effective atomic number ($Z_{eff} = 13$) than soft tissue ($Z_{eff} = 7$), due to its high concentration of calcium (Z = 20) and phosphorus (Z = 15), bones produce high contrast on X-ray image modalities [61].
There are four major types of interactions of X- and gamma-ray photons with matter, the first three of which play a role in diagnostic radiology and nuclear medicine: (a) Rayleigh scattering, (b) Compton scattering, (c) photoelectric absorption, and (d) pair production. In tissue the predominant attenuator process are Compton scattering and photo-electric effect $A.1$.
The photoelectric process predominates when lower energy photons interact with high Z materials , figure $A.2$. In fact, photoelectric absorption is the primary mode of interaction of diagnostic X-rays with screen phosphors, radiographic contrast materials, and bone [61]. Conversely, Compton scattering will predominate at most diagnostic photon energies in materials of lower atomic number such as tissue and air.

A.0.1 Compton effect

Compton scattering occur between photons and outer shell electrons, figure $A.3$.
Compton scattering results in the ionization of the atom and a division of the incident photon energy between the scattered photon and ejected electron. The electron is ejected from the atom, and the photon is scattered with some reduction in energy. As with all types of interactions, both energy and momentum must be conserved. Thus the energy of the incident photon (E_0) is equal to the sum of the energy of the scattered photon (E_{sc}) and the kinetic energy of the ejected electron (E_{e^-}) as shows in Eq. $A.1$.

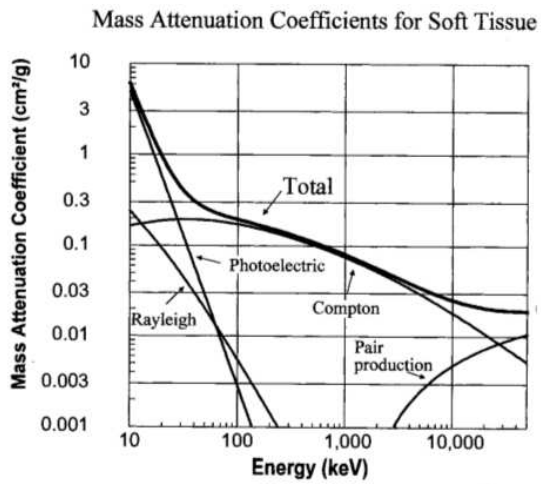

Figure A.1: Graph of the Rayleigh, photoelectric, Compton, pair production, and total mass attenuation coefficients for soft tissue (Z = 7) as a function of energy.[61]

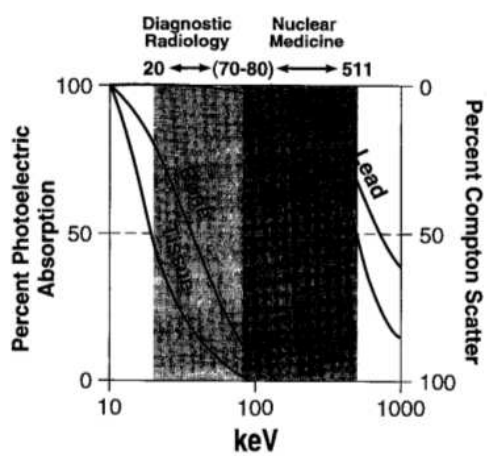

Figure A.2: Graph of the percentage of contribution of photoelectric (left scale) and Compton (right scale) attenuation processes for various materials as a function of energy. When diagnostic energy photons (i.e., diagnostic x-ray effective energy of 20 to 80 keV; nuclear medicine imaging photons of 70 to 511 keV), interact with materials of low atomic number (e.g., soft tissue), the Compton process dominates. [61]

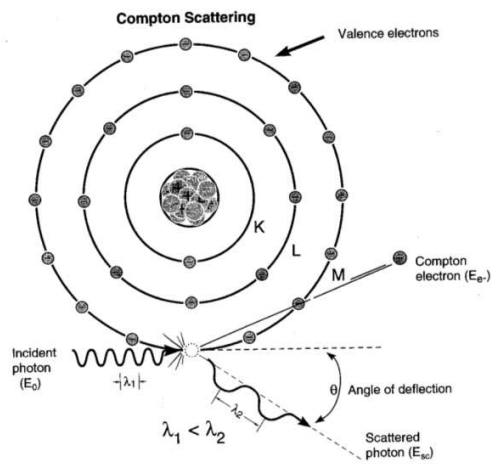

Figure A.3: Compton scattering Diagram. [61]

The ejected electron will lose its kinetic energy via excitation and ionization of atoms in the surrounding material.

$$E_0 = E_{sc} + E_{e^-} \tag{A.1}$$

The energy of the scattered photon can be calculated from the energy of the incident photon and the angle of the scattered photon (with respect to the incident trajectory) as

$$E_{sc} = \frac{E_0}{1 + \frac{E_0}{511keV}(1 + cos\theta)} \tag{A.2}$$

where θ is the angle of scattered photon. As the incident photon energy increases, both scattered photons and electrons are scattered more toward the forward direction. In addition, for a given scattering angle, the fraction of energy transferred to the scattered photon decreases with increasing incident photon energy. Thus, for higher energy incident photons, the majority of the energy is transferred to the scattered electron. Compton interaction also depends on the electron density (number of electrons/g X density). With the exception of hydrogen, the total number of electrons/g is fairly constant in tissue; thus, the probability of Compton scattering per unit mass is nearly independent of Z, and the probability of Compton scattering per unit volume is approximately proportional to the density of the material. Compared to other elements, the absence of neutrons in the hydrogen atom results in an approximate doubling of electron density. Thus, hydrogenous materials have a higher probability of Compton scattering than a nonhydrogenous material of equal mass [61].

A.0.2 Photoelectric effect

In the photoelectric effect, all of the incident photon energy is transferred to an electron, which is ejected from the atom. The kinetic energy of the ejected photo-electron (E_e)

is equal to the incident photon energy (E_o) minus the binding energy of the orbital electron (E_b), figure. In order for photoelectric absorption to occur, the incident photon energy must be greater than or equal to the binding energy of the electron that is ejected.

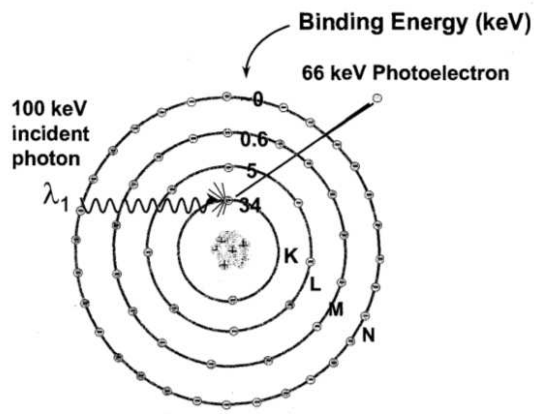

Figure A.4: Photoelectric absorption. A 100 keV photon is undergoing photoelectric absorption whit an iodine atom. In this case the K-sell electron is ejected with a kinetic energy equal to the incident photon energy and the k-shell biding energy of 34 or 66 keV. [61]

The probability of photoelectric absorption per unit mass is approximately proportional to Z^3/E^3, where Z is the atomic number and E is the energy of the incident photon. For example, the photoelectric interaction probability in iodine (Z =53) is $(53/20)^3$ or 18.6 times greater than in calcium (Z = 20) for photon of a particular energy [61]. A photon cannot undergo a photoelectric interaction with an electron in a particular atomic shell or subshell if the photon's energy is less than the binding energy of that shell or subshell. This causes the dramatic decrease in the probability of photoelectric absorption for photons whose energies are just below the binding energy of a shell. Thus, the photon energy corresponding to an absorption edge is the binding energy of the electrons in that particular shell or subshell. For example, the primary elements comprising soft tissue (H, C, N, and 0) have absorption edges below 1 keV [61]. At photon energies below 50 keV the photoelectric effect plays an important role in imaging soft tissue. The photoelectric absorption process can be used to amplify differences in attenuation between tissues with slightly different atomic numbers, thereby improving image contrast [61].

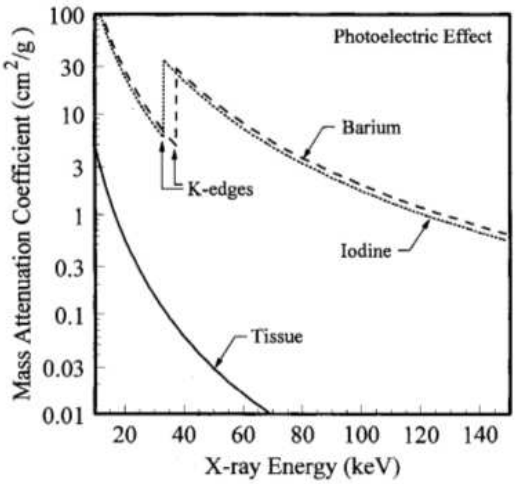

Figure A.5: Photoelectric mass attenuation coefficients for tissue (Z=7), iodine (Z= 53), and barium (Z = 56) as a function of energy. Abrupt increase in the attenuation coefficients called ”absorption edges” occur due to increased probability of photoelectric absorption when the photon energy just exceeds the binding energy of inner shell electrons (e.g., K, L, M. ..) thus increasing the number of electrons available for interaction. This process is very significant for high-Z material, such as iodine and barium, in the diagnostic energy range. [61]

Glossary

coherent light light in which the electromagnetic waves maintain a fixed and predictable phase relationship with each other over a period of time.. 8, 12

N total number of complex phasors from N scatters.. 13

phasor complex number used to represent sinusoidal function on time.. 11

Probability Density Function Let X be a continuous random variable. Then a probability density function (pdf) of X is a function f(x) such that for any two numbers a and b with $a \leq b$,

$$P(a \leq X \leq b) = \int_a^b f(x)dx \tag{A.3}$$

That is, the probability that X takes on a value in the interval [a,b] is the area above this interval and under the graph of the density function.. 13, 14

randomly Of or characterizing a process of selection in which each item of a set has an equal probability of being chosen.. 8

statistically stationary A stationary process has the property that the mean, variance and autocorrelation structure do not change over time.. 9

stochastic a statistical process involving a number of random variables depending on a variable parameter.. 8

Acronyms

σ standard deviation. 4

τ time which the degree complex of coherence decrease monotonically. 10, 11, 19

μ_a absorption coefficient. 2, 3

μ_s scattering coefficient. 3

$G(\tau)$ Autocorrelation function. 11, 19

$G^{(2)}(\xi - \xi^{'})$ Second order of autocorrelation function. 19

$I(\vec{r}, t)$ Intensity as a position and time function. 9

$U(\vec{r},t)$ complex amplitude. 8, 9

$U(t)$ stationary light fluctuations function. 10

d_{min} speckle size. 16

$u(\vec{r}, t) = Re\{U(\vec{r},t)\}$ arbitrary wavefunction. 8, 9

C speckle contrast. 4

g anisotropy factor. 3

LSI Laser Speckle Imaging. 1, 2, 3, 6

mLSI modified Laser Speckle Imaging. 4, 5, 6

TiBS Trans-illumination Breast Spectroscopy. 6

W Time-integrated intensity. 18

List of Figures

1.1 Schematic illustration of photons reflection, absorption scattering and transmission in a tissue sample. 2
1.2 Comparison of fourth most common absorbers in tissue and the Mie scattering [5]. 3
1.3 Sinple image of speckle pattern. 4
1.4 Blurring in the speckle pattern. 5
1.5 Velocity map of the laser speckle image of the roedent brain calculated by spatial analisys. Velocity map of the laser speckle image of the roedent brain calculated by temporal analisys [7]. 6

2.1 Random scattering by tissue components. 9
2.2 Waves statistically stationary (a) and statistically nonstationary (b).[18] 10
2.3 Variation of the phasor $U(t)$ with time when its argument is uniformly distributed between 0 and 2π. The average values of its real and imaginary parts are zero, so that $\langle U(t)\rangle = 0$. [18]. 11
2.4 Magnitude of the complex degree of temporal coherence $g(\tau)$, and the coherence time τ_c for an optical field with short (left) coherence time and long coherence time (right). [18] 12
2.5 Examples of the magnitude of the normalized mutual intensity as a function of $\vec{r}_l$ in the vicinity of a fixed point $\vec{r}_2$. The coherence area in (a) is smaller than that in (b). Bahaa E. A. Saleh, *Fundamentals of Photonics*, Chapter 10. Copyright John Wiley & Sons, Inc. (1991). 14
2.6 Resultant phasor amplitude U. 14
2.7 Objective speckle set-up 17
2.8 Subjective speckle set-up 17
2.9 Optical system to produce speckle pattern from a diffuse object. 25
2.10 Spatial statistics of a time-integrated speckle. 27
2.11 Temporal statistics of a time-integrated speckle. 28

3.1 Sensitivity as function of the number of coherence intervals captured over unit of time $(i.e., 1/N_t)$. 31
3.2 Simple representation of the experimental setup employed in this experiment. 32

3.3 (a) Both SFI and $1/N_t$ values maintain a linear relationship to the actual flow rate, for an actual flow rate greater than $5mm/s$ and image exposure time of $1ms$. For an actual flow rate less than $5mm/s$, it is necessary to employ a longer exposure time to achieve a linear response, as demonstrated in (b) for $T = 10ms$. 34
3.4 (a) $1/N_t$ and (b) SFI values as a function of the actual velocity, for four exposure times (T). Note that, for a given actual flow rate, the $1/N_t$ value depends on exposure time, while the SFI value is unaffected. 34
3.5 Maps of in vitro flow rates predicted with the mLSI model for actual flow rates of (a) 10mm/s and (b) 3mm/s. 35
3.6 Maps of in vitro flow rate predicted with our modified mLSI model (equation 3.5) for actual flow rates of (a) $10mm/s$ and (b) $3mm/s$. Exposure times of 1 and $10ms$ were used to work within the linear response range of our instrument for the two actual flow rates. 35

4.1 Skin phantom employed in this study. Intralipid was injected into the inlet, and K (contrast) and SFI (Speckle Flow Index) measurements were determined at regions within channels C1 and C3 39
4.2 Experimental setup. 40
4.3 Average speckle contrast of a region within channel C1, vs. flow speed, for different ratios of spatial sampling of the speckle pattern (e.g., pixels-per-speckle values) for (a) temporal and (b) spatial speckle contrast analysis. The symbols represent experimental data and the solid lines are the corresponding fits to Eq. 4.4. 41
4.4 Relative flow speed [e.g., (SFI in C1)/(SFI in C3)] is only weakly dependent on N and actual flow speed. The dependence is noticeably weaker with the (a) temporal speckle contrast approach than with the (b) spatial speckle contrast approach. 42
4.5 Relative flow speed [e.g., (SFI in C1)/(SFI in C3)] is only weakly dependent on N and actual flow speed. The dependence is noticeably weaker with the (a) temporal speckle contrast approach than with the (b) spatial speckle contrast approach. 42
4.6 RFS as function of x for different values of ρ, while the RFS for the temporal algorithm keeps constant around 2 for different values of ρ (continuous line), the RFV for the spatial algorithms is very sensitive to any change of this parameter, i.e. it is very sensitive to the static light even as small as 1% of the total light. 44

5.1 Breast Cancer. Incidence/Mortality Worldwide in 2012 46
5.2 Breast Cancer. Mexico Incidence/Mortality in 2012 46
5.3 Incidence of malignant breast tumor in women aged 20 years and over by age group, 2011. 47

5.4 Breast Cancer hospital case fatality rate, in women of 20 years and more by age group, 2012. 47
5.5 Lateral view of the female breast, Adapted from [54]. 48
5.6 Light-tissue interaction. 51
5.7 Chromophores present in biological tissues and their absorption spectra. 53
5.8 Flowchart algorithm to calculate the chromophore concentration $[c]_S$. . 54
5.9 Fit$F(\lambda)$, and actual $S(\lambda)$ spectrum. 55
5.10 We show that white block correction spectrum is not reproducible by using the pinhole as raw source spectrum because this varies with the position in which the pinhole is 57
5.11 The white block spectrum measured with the TiBS system (continous line) and the spectrum measured with the lasers (points). Data provided by Jane Walter. 58
5.12 Chromophere average and standard deviation. 59

A.1 Graph of the Rayleigh, photoelectric, Compton, pair production, and total mass attenuation coefficients for soft tissue (Z = 7) as a function of energy.[61] 61
A.2 Graph of the percentage of contribution of photoelectric (left scale) and Compton (right scale) attenuation processes for various materials as a function of energy. When diagnostic energy photons (i.e., diagnostic x-ray effective energy of 20 to 80 keV; nuclear medicine imaging photons of 70 to 511 keV), interact with materials of low atomic number (e.g., soft tissue), the Compton process dominates. [61] 61
A.3 Compton scattering Diagram. [61] 62
A.4 Photoelectric absorption. A 100 keV photon is undergoing photoelectric absorption whit an iodine atom. In this case the K-sell electron is ejected with a kinetic energy equal to the incident photon energy and the k-shell biding energy of 34 or 66 keV. [61] 63
A.5 Photoelectric mass attenuation coefficients for tissue (Z=7), iodine (Z= 53), and barium (Z = 56) as a function of energy. Abrupt increase in the attenuation coefficients called ”absorption edges” occur due to increased probability of photoelectric absorption when the photon energy just exceeds the binding energy of inner shell electrons (e.g., K, L, M. ..) thus increasing the number of electrons available for interaction. This process is very significant for high-Z material, such as iodine and barium, in the diagnostic energy range. [61] 64

List of Tables

3.1 Relative flow rate change and % relative error predicted by the equations (1) and (6) from figures 4 and 5 respectively. 36
3.2 Relative flow rate change and % relative error predicted with equations (1) and (5). 36

Bibliography

[1] D. Attwell, A. M. Buchan, S. Charpak, M. Lauritzen, B. A. MacVicar and E. A. Newman *Glial and neuronal control of brain blood flow* Nature 468, 232?243 (2010).

[2] J. Kur, E. A. Newman, and T. Chan-Ling *Cellular and physiological mechanisms underlying blood flow regulation in the retina choroid in health disease* Prog Retin Eye Res. 31, 377?406. (2012).

[3] G. T. Feke *Laser Doppler instrumentation for the measurement of retinal blood flow: theory and practice* Bull Soc Belge Ophtalmol. 302, 171-84 (2006).

[4] A. J. Welch, M. J. C. van Gemert *Optical-Thermal Response of Laser-Irradiated Tissuee* Springer, Second Edition (2011).

[5] M. R. Hamblin, Y-Y. Huang *Handbook of Photomedicine* CRC Press (2014).

[6] G. Michelson, B. Schmauss, M. J. Langhans, J. Harazny, M. J. Groh.*Principle, validity, and reliability of scanning laser Doppler flowmetry* J Glaucoma. 5, 99-105, (1996).

[7] Y. Cheng , Q. M. Luo, S. Q. Zeng, S. B. Chen, J. Cen and H. Gong *Modified laser speckle imaging method with improved spatial resolution* J. Biomed. Opt. 8 559-64 (2003)

[8] S. Yuan, A. Devor , D, A. Boas and A. K. Dunn *Determination of optimal exposure time for imaging of blood flow changes with laser speckle contrast imaging* Appl. Opt. 44 1823?30 (2005)

[9] A. Fercher and J. Briers, *Flow visualization by means of single-exposure speckle photography*. Opt. Commun. 37, 326?330 (1981).

[10] M. Hirao, H. Oku, W. Goto,T. Sugiyama ,T. Kobayashi and T. Ikeda *Effects of adenosine on optic nerve head circulation in rabbits* Exp. Eye Res. 79 729?35 (2004)

[11] K. R. Forrester, J. Tulip, C. Leonard , C. Stewart and R. C. Bray *Laser speckle imaging technique for measuring tissue perfusion* IEEE Trans. Biomed. Eng. 51 2074?84 (2004)

[12] T. K. Smith, B. Choi ,J. C. Ramirez-San-Juan, J. S. Nelson, K. Osann and K. M. Kelly *Microvascular blood flow dynamics associated with photodynamic therapy and pulsed dye laser irradiation* Lasers Surg. Med. 38 532?9 (2006)

[13] B. Choi, N. M. Kang and J. S. Nelson *Laser speckle imaging for monitoring blood flow dynamics in the in vivo rodent dorsal skinfold model* Microvasc. Res. 68 143?6 (2004)

[14] A. I. Srienc, Z. L. Kurth-Nelson and E. A. Newman *Imaging retinal blood flow with laser speckle flowmetry* Forntiers in Neuroenergetics 2 (128) 1-10 (2010)

[15] J. C. Dainty *Lser Speckle and Related Phenomena* Ed. Springer-Verlag, (1984).

[16] S. Webster and J. D. Briers, *Time-integrated speckle for the examination of movement in biological systems*. Proc. SPIE 2132, 444-52, 1994.

[17] A. K. Dunn , A. Devor, A. M. Dale and D. A. Boas *Spatial extent of oxygen metabolism and hemodynamic changes during functional activation of the rat somatosensory cortex* Neuroimage 27 279?90 (2005)

[18] Bahaa E. A. Saleh, *Fundamentals of Photonics*, Chapter 10. John Wiley & Sons, Inc. (1991).

[19] E. Hecht, *Optics*. Addison Wesley, 1987.

[20] J. W. Goodman, *Statistical Optics*. John Wiley & Sons, 2000.

[21] J. W. Goodman, *Some fundamental properties of speckle*. J. Opt. Soc. Am. 66, 1145-1150 (1976).

[22] J. W. Goodman, *Statistical properties of laser speckle patterns* in Laser speckle and related phenomena. J. C. Dainty, Ed. Springer-Verlag, 1984.

[23] J. W. Goodman, *Speckle Phenomena in Optics: Theory and Applications* Version 8.0

[24] M. M. Siddiqui, *Statistical inference for Rayleigh distributions.*, Radio Science, 68D, 1007, (1964).

[25] J. C. Dainty, *The statistic of speckle patterns in Progress in Optics XIV*.North-Holland, 1976.

[26] L. Mandel and E. Wolf, *Coherence Properties of Optical Fields*. Rev. Mod. Phys., 37:231, 1965.

[27] G. Cloud, *Optical Methods*. Journal Compilation, 2007.

[28] R. Bandyopadhyay, A. Gittings, S. Suh, P. Dixon, and D. Durian, *Speckle-visibility spectroscopy: A tool to study time-varying dynamics*. Rev. Sci. Instrum. 76, 093110 2005.

[29] J. C. Ramirez San Juan, *Simple correlation factor for Laser Speckle Imaging of flow dynamics*, Optics Letters 39, 3, 678-681 2014.

[30] A. B. Parthasarathy, W. J. Tom, A. Gopal, X. Zhang and A. K. Dunn,*Robust flow measurement with multi-exposure speckle imaging*. Opt. Express 16, 3, 1975-89, 2008.

[31] D. A. Boas, *Diffuse Photon Probes of Structural and Dynamical Properties of Turbid Media: Theory and Biomedical Applications*. Ph. D. dissertation (Department of Physics and Astronomy, University of Pennsylvania, Philadelphia, Pa. 1996).

[32] H. Cheng, Q. Luo, S. Zeng, S. Chen, J. Cen and H. Gong, *Modified laser speckle imaging method with improved spatial resolution*. J. Biomed. Opt. 8, 559?64,2003.

[33] H. Cheng, Y. Yan and T. Duong, *Temporal statistical analysis of laser speckle imaging and its applications to retinal blood-flow imaging*. Opt. Express 16 10214?9, 2008.

[34] J. Ohtsubo and T. Asakura, *Velocity measurement of a diffuse object by using time-varying speckles*. Opt. Quant. Electron. 8, 523?529, 1976.

[35] N. Takai, *Scattering of Gaussian laser beam by flow particles*. Bulletin of the Faculty of Engineering, Hokkaido University, No.85, 1977.

[36] J. D. Briers and S. Webster, *Laser Speckle Contrast Analysis (LASCA): a Non-scanning, Full-Field Technique For Monitoring Capillary Blood Flow*. J. Biomed. Opt. 1, 174-79, 1996.

[37] J. C. Ramirez-San-Juan, R. Ramos-Garcia, I. Guizar-Iturbide, G. Martinez-Niconoff, and B. Choib,*Impact of velocity distribution assumption on simplified laser speckle imaging equation* Opt. Express 16(5), 3197-3203 (2008)

[38] B. Choi, J. C. Ramirez-San-Juan, J. Lotfi and J. S. Nelson. *Linear response range characterization and in vivo application of laser speckle imaging of blood flow dynamics* J. Biomed. Opt. 11, 041129 (2006).

[39] S. Yuan, A. Devor , D. A. Boas and A. K. Dunn. *Determination of optimal exposure time for imaging of blood flow changes with laser speckle contrast imaging* Appl. Opt. 44 1823-1830 (2005).

[40] A. K. Dunn, A. Devor , A. M. Dale and D. A. Boas. *Spatial extent of oxygen metabolism and hemodynamic changes during functional activation of the rat somatosensory cortex* Neuroimage 27 279-290 (2005).

[41] S. J. Kirkpatrick, D. Duncan *Detrimental effects of speckle-pixel size matching in laser speckle contrast imaging* Opt. Lett. 33 2886-2888 (2008).

[42] B. Choi, N.M Kang and J. S. Nelson *Laser speckle imaging for monitoring blood flow dynamics in the in vivo rodent dorsal skinfold model* Microvasc. Res. 68 143-146 (2004)

[43] B. Choi, J. C. Ramirez-San-Juan, J.Lotfi and J. S. Nelson *Linear response range characterization and in vivo application of laser speckle imaging of blood flow dynamics* J. Biomed. Opt. 11 041129 (2006)

[44] O. Thompson, M. Andrews, and E. Hirst, *Correction for spatial averaging in laser speckle contrast analysis* Biomed. Opt. Express 2(4), 1021-1029 (2011).

[45] A. Ennos, *Speckle interferometry*, in Laser Speckle and Related Phenomena, J.C. Dainty (Springer-Verlag) 11.

[46] D.A. Boas and A,K. Dunn, *Laser speckle contrast imaging in biomedical optics* J. Biomed. Opt. 15 011109 (2010).

[47] P.A. Lemieux and D. J. Durian, *Investigating non-Gaussian scattering process by using nth-order intensity correlation function* J. Opt. Soc. Am. A 16 1651-1664 (1999).

[48] Y. Atchia, H. Levy, S. Dufour, and O. Levi, *Rapid multiexposure in vivo brain imaging system using vertical cavity surface emitting lasers as a light source* Applied Optics 52, 7,(2013).

[49] K. Basak, M. Manjunatha and P. Dutta, *Review of laser speckle-based analysis in medical imaging* Med Biol Eng Comput. 50 547-58 (2012).

[50] D. Duncan, J. Kirkpatrick and K. Wang, *Statistics of local speckle contrast* J. Opt. Soc. Am. A 25 9-15 (2008).

[51] M. K. Simick *Near Infrared Trans-illumination Spectroscopy of Breast Tissue for Correlation with Mammographic Densityt* Masters of Science Thesis, Department of Medical Biophysics University of Toronto (2002).

[52] World Health Organization *http://globocan.iarc.fr/Pages/fact sheets cancer.aspx*

[53] Instituto Nacional de Estadistica y Geografia, *Estadisticas a proposito del dia internacional contra el cancer de mama*(2013)

[54] Anatomy of the breast *http://learnpediatrics.com/body-systems/neonate/breastfeeding-problems/*

[55] A. Leproux, PhD thesis *Breast lesion detection using diffuse optical imaging* AMC-UvA. 2012

[56] N. F. Boyd, H.Guo , L. J. Martin, et al. *Mammographic density and the risk and detection of breast cancer* N Engl J Med. 356, 227-36, (2007).

[57] R. M. Tamimi, C. Byrne, G. A. Colditz, S. E. Hankinson*Endogenous hormone levels, mammographic density, and subsequent risk of breast cancer in post-menopausal women*, J Natl Cancer Inst. 99, 1178-87, (2007).

[58] Screening and Testing *http://www.breastcancer.org/symptoms/testing/types*

[59] Lihohg V. Wang and Hsin-I Wu, *Biomedical Optics: Principles and Imaging* Wile (2007)

[60] J. H. Mathews and K. K. Fink *Numerical Methods Using Matlab: Nelder-Mead Method* Prentice-Hall Inc. (2004)

[61] J. T. Bushberg et. al. *The Essential Physics of Medical Imaging* Lippincott Williams & Wilkins, (2002).